

Neogene cooling driven by land surface reactivity rather than increased weathering fluxes

Jeremy K. Caves Rugestein^{1,5,6*}, Daniel E. Ibarra² & Friedhelm von Blanckenburg^{3,4}

The long-term cooling, decline in the partial pressure of carbon dioxide, and the establishment of permanent polar ice sheets during the Neogene period^{1,2} have frequently been attributed to increased uplift and erosion of mountains and consequent increases in silicate weathering, which removes atmospheric carbon dioxide^{3,4}. However, geological records of erosion rates are potentially subject to averaging biases^{5,6}, and the magnitude of the increase in weathering fluxes—and even its existence—remain debated^{7–9}. Moreover, an increase in weathering scaled to the proposed erosional increase would have removed nearly all carbon from the atmosphere¹⁰, which has led to suggestions of compensatory carbon fluxes^{11–13} in order to preserve mass balance in the carbon cycle. Alternatively, an increase in land surface reactivity—resulting from greater fresh-mineral surface area or an increase in the supply of reactive minerals—rather than an increase in the weathering flux, has been proposed to reconcile these disparate views^{8,9}. Here we use a parsimonious carbon cycle model that tracks two weathering-sensitive isotopic tracers (stable ⁷Li/⁶Li and cosmogenic ¹⁰Be/⁹Be) to show that an increase in land surface reactivity is necessary to simultaneously decrease atmospheric carbon dioxide, increase seawater ⁷Li/⁶Li and retain constant seawater ¹⁰Be/⁹Be over the past 16 million years. We find that the global silicate weathering flux remained constant, even as the global silicate weathering intensity—the fraction of the total denudation flux that is derived from silicate weathering—decreased, sustained by an increase in erosion. Long-term cooling during the Neogene thus reflects a change in the partitioning of denudation into weathering and erosion. Variable partitioning of denudation and consequent changes in silicate weathering intensity reconcile marine isotope and erosion records with the need to maintain mass balance in the carbon cycle and without requiring increases in the silicate weathering flux.

Sedimentary records suggest that global erosion rates have increased by a factor of between two and ten since the Miocene epoch^{4,14,15}, and a global compilation of thermochronometry-derived exhumation rates indicates that mountain erosion has increased by a factor of two to four over the past 8 million years (Myr)¹⁶. Because greater erosion fluxes are correlated with higher weathering fluxes^{17,18}, increasing marine ⁸⁷Sr/⁸⁶Sr has been proffered as evidence of corresponding increases in the silicate weathering flux, thereby cooling the climate over the Neogene³. Because the reservoir of carbon in the ocean–atmosphere system is extremely small relative to the weathering flux over the Neogene¹⁰, several speculative compensatory fluxes of carbon—including enhanced oxidation of organic carbon relative to burial¹¹, erosion-driven increases in sulfide oxidation¹², and/or declining island-arc basalt weathering¹³—have been proposed to reconcile the erosion-driven increase in weathering with the need to preserve mass balance in the carbon cycle. However, each of these proposed mechanisms centres upon the notion that increasing marine ⁸⁷Sr/⁸⁶Sr represents an increase in the silicate weathering flux in the Neogene. The value of marine ⁸⁷Sr/⁸⁶Sr as a tracer of the global silicate weathering flux, however, is questionable, and it has been shown to relate more

closely to the ⁸⁷Sr/⁸⁶Sr composition of bulk rock undergoing weathering¹⁹. An alternative proxy record—the marine record of ¹⁰Be/⁹Be—has been used to suggest a constant global silicate weathering flux over the past 12 Myr⁷. However, a constant weathering flux alone cannot explain the simultaneous decrease in the partial pressure of carbon dioxide (p_{CO_2}) or why weathering remained constant even as the climate cooled.

Because the silicate weathering flux acts as a negative feedback on climate, changes in p_{CO_2} lead to changes in atmospheric temperature and runoff, which in turn modify weathering fluxes²⁰. In contrast to the hypotheses above that rely upon changing weathering fluxes to explain cooling, an increase in the efficiency of the silicate weathering sink of CO₂ results in more efficient removal of carbon, subsequently lower p_{CO_2} (refs 9,10) and a decrease in the intensity with which rock is weathered to soil, without changes in weathering fluxes. However, there are few direct data to constrain the precise mechanism by which such an efficiency change is mediated. To identify such a mechanism, we combine two promising marine isotope proxies—the ratio of stable ⁷Li to ⁶Li (⁷Li/⁶Li, denoted as $\delta^7\text{Li}$), which records the relative amount of clay formed during terrestrial weathering and thus the silicate weathering intensity^{21,22}; and the ratio of the cosmogenic ¹⁰Be (meteoric) to stable ⁹Be (¹⁰Be/⁹Be), which records the silicate weathering flux into a given ocean basin²³—and embed the weathering zone processes of these isotope proxies into a long-term model of the carbon cycle (Fig. 1). We use this model to determine the geologic forcings required to match the Neogene marine $\delta^7\text{Li}$ and ¹⁰Be/⁹Be records and the atmospheric p_{CO_2} record.

We adapt our forward carbon cycle model (CLiBeSO-W: carbon-lithium-beryllium-sulfur-oxygen weathering model) from ref. 24, which is a simplified version of the COPSE and GEOCARBSULF models²⁰ (see Methods). CLiBeSO-W tracks the reservoirs of carbon (C) and alkalinity (A) as a function of the major fluxes of C and A between the solid Earth and the ocean–atmosphere system, including volcanic and solid Earth degassing; weathering and burial of carbonate, organic carbon and pyrite; and silicate weathering. The weathering fluxes are a function of erosion, and the silicate and carbonate weathering fluxes are also sensitive to climate; this is demonstrated in equation (1), which describes the dependence between the silicate weathering flux (F_{silw}) and erosion (E) and climate (represented by p_{CO_2}):

$$F_{\text{silw}} = \left(\frac{E}{E_0} \right)^{\alpha_{\text{sil}}} k_1 (\log_2(R_{\text{CO}_2}) + 1) \quad (1)$$

Here, α_{sil} permits a nonlinear response between erosion and weathering, k_1 is a constant that encompasses the factors that control land surface reactivity independent of erosion (for example, exposed lithologies and vegetative cover), E_0 is the erosion rate at 16 Myr ago, and R_{CO_2} is the ratio of p_{CO_2} at time t in the model to pre-industrial levels of p_{CO_2} . We use a \log_2 climatic response owing to the logarithmic scaling of surface temperature with p_{CO_2} (ref. 25). Equation (1) encapsulates

¹Department of Earth Sciences, ETH Zürich, Zürich, Switzerland. ²Department of Geological Sciences, Stanford University, Stanford, CA, USA. ³GFZ German Research Centre for Geosciences, Earth Surface Geochemistry, Potsdam, Germany. ⁴Institute of Geological Sciences, Freie Universität Berlin, Berlin, Germany. ⁵Present address: Max Planck Institute for Meteorology, Hamburg, Germany. ⁶Present address: Senckenberg Biodiversity and Climate Research Centre, Frankfurt, Germany. *e-mail: jeremy.rugestein@mpimet.mpg.de

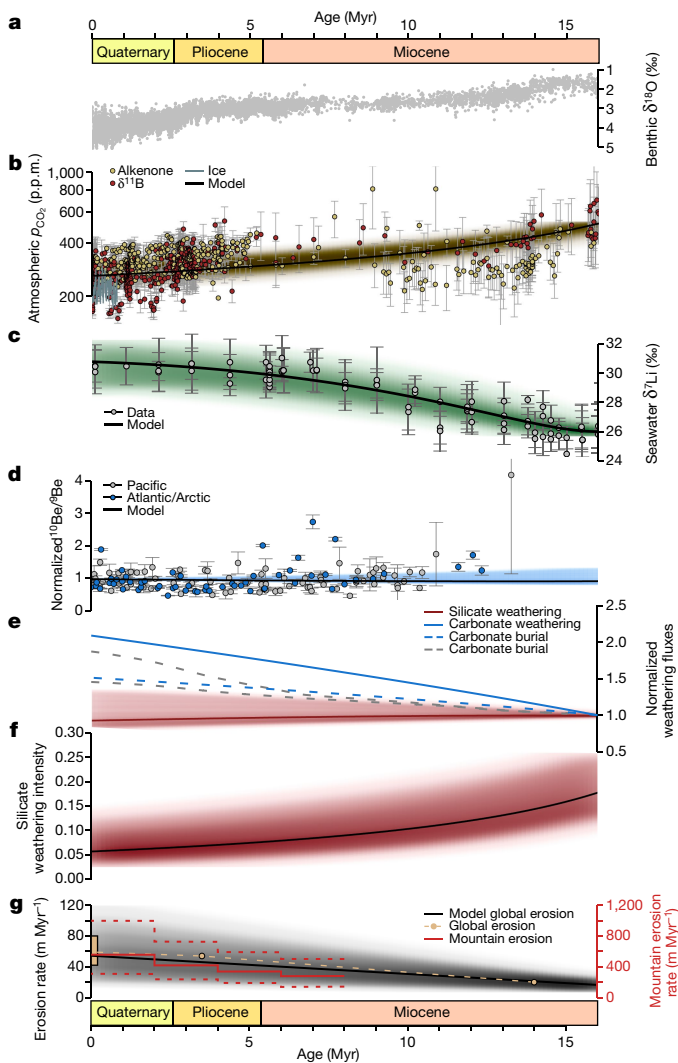


Fig. 1 | Weathering and carbon cycle results of the CLiBeSO-W model from 16 Myr ago to 0 Myr ago. Model output using the mean of the MCMC optimized parameters is shown by the black lines; shading indicates the density of all convergent MCMC iterations. **a**, Benthic foraminifera $\delta^{18}\text{O}$ as a proxy of deep-ocean temperature and ice volume¹. **b**, Atmospheric p_{CO_2} with alkenone (yellow) and $\delta^{11}\text{B}$ (red) proxy and ice-core data (see Methods). **c**, Modelled seawater $\delta^7\text{Li}$. The grey points are data from planktonic foraminifera $\delta^7\text{Li}$ (ref. 28). **d**, Modelled marine $^{10}\text{Be}/^9\text{Be}$, normalized to the value at 0 Myr ago. Grey and blue points are reconstructed marine $^{10}\text{Be}/^9\text{Be}$ data from ref. 7, normalized to the modern $^{10}\text{Be}/^9\text{Be}$ value of the respective ocean basin. **e**, Normalized silicate (red) and carbonate (blue) weathering flux and carbonate burial (dashed blue) flux. The grey dashed lines are the estimated minimum and maximum changes in carbonate burial from sedimentary volumes³⁰. **f**, Silicate weathering intensity ($F_{\text{silw}}/(E + F_{\text{silw}})$). **g**, Globally averaged erosion rate (left axis). The solid, lower dashed and upper dashed red lines show the mean, minimum and maximum mountain erosion rate estimates, respectively¹⁶ (right axis). The beige dashed line is an estimate of the global erosion rate¹⁵ and the beige bar at 0 Myr ago indicates the full range of estimated pre-anthropogenic erosion rates^{15,18} (left axis). In **b–d**, error bars are the published uncertainty for the data (minimum/maximum in **b**, 1σ in **c**, **d**).

the silicate weathering feedback: to balance carbon input fluxes, changes in the $\left(\frac{E}{E_0}\right)^{\alpha_{\text{sil}}}$ term must be matched by simultaneous changes in the $(\log_2(R_{\text{CO}_2}) + 1)$ term. The combination of E/E_0 and k_1 represents the efficiency of this feedback⁹. We show below that this feedback strength is governed by land surface reactivity, which is maintained by erosion.

Marine $^{10}\text{Be}/^9\text{Be}$ (denoted $(^{10}\text{Be}/^9\text{Be})_{\text{oc}}$) is set by the ratio of the downward flux (F_{met}) of radioactive, meteoric ^{10}Be (with a half-life of 1.4 Myr and produced in the atmosphere by the bombardment of atmospheric molecules by cosmic rays) to the upward, exhumation flux of ^9Be that is released by silicate weathering²³ (carbonates have a negligible Be content)²⁶:

$$\left(\frac{^{10}\text{Be}}{^9\text{Be}}\right)_{\text{oc}} = \frac{R_{\text{area}}F_{\text{met}} + \varphi_{\text{del}}F_{\text{met}}}{\varphi_{\text{del}}F_{\text{silw}}[\text{Be}]} \quad (2)$$

where R_{area} is the ratio of oceanic to land surface area, φ_{del} is the fraction of Be that is ultimately delivered to the ocean by rivers, and $[\text{Be}]$ is the average concentration of Be in bedrock. Assuming that R_{area} , F_{met} and φ_{del} are approximately constant, a higher $^{10}\text{Be}/^9\text{Be}$ reflects a lower weathering flux.

In contrast to $^{10}\text{Be}/^9\text{Be}$, which is sensitive to the silicate weathering flux, $\delta^7\text{Li}$ records the relative amount of clay formed during weathering and thus the silicate weathering intensity^{21,22}, which is defined as $F_{\text{silw}}/(E + F_{\text{silw}})$. We assume that there is no major fractionation of ^7Li during primary mineral dissolution, but that secondary mineral formation involves a large fractionation ($\Delta_{\text{sec}} = -17\text{‰}$ (ref. 22)), such that ^6Li is preferentially incorporated into secondary minerals whereas ^7Li is partitioned into the soil water. In settings that have a high weathering intensity (that is, where F_{silw} is roughly equivalent to E), Li is quantitatively weathered from the regolith and clays are dissolved, resulting in a riverine $\delta^7\text{Li}$ flux that resembles rock $\delta^7\text{Li}$. In environments that have a low weathering intensity (that is, where $E \gg F_{\text{silw}}$), secondary mineral formation is limited and thus riverine $\delta^7\text{Li}$ also reflects rock $\delta^7\text{Li}$. Consequently, a hump-shaped dependence between weathering intensity and $\delta^7\text{Li}$ emerges (Fig. 2), in which the highest $\delta^7\text{Li}$ in river waters occurs at intermediate weathering intensity, where secondary minerals are both formed and eroded sufficiently fast so as to inhibit their re-dissolution^{21,22}. We thus parameterize riverine $\delta^7\text{Li}$ ($\delta^7\text{Li}_{\text{riv}}$) as a function of weathering intensity, as reflected by the ratio of E to F_{silw} , adapted from ref. 21:

$$\delta^7\text{Li}_{\text{riv}} = -\frac{E}{F_{\text{silw}}}(\delta^7\text{Li}_{\text{sed}} - \delta^7\text{Li}_{\text{rock}}) + \delta^7\text{Li}_{\text{rock}} \quad (3)$$

where average $\delta^7\text{Li}_{\text{rock}}$ is approximately 1.5‰ (ref. 27), and $\delta^7\text{Li}_{\text{sed}}$ represents the Li isotopic composition of exported sediments, including both secondary and primary minerals (Fig. 2) (for a full derivation of equation (3), calculation of bulk weathering and erosion, and constraints on $\delta^7\text{Li}_{\text{sed}}$ for equation (3), see Methods). To predict paleo-seawater $\delta^7\text{Li}$ ($\delta^7\text{Li}_{\text{oc}}$), we use an embedded box-model of the marine lithium cycle²⁸.

To estimate the change in erosion that is necessary to match records of seawater $\delta^7\text{Li}$, $^{10}\text{Be}/^9\text{Be}$, and atmospheric p_{CO_2} over the past 16 Myr, we use a Markov chain Monte Carlo (MCMC) method to minimize the misfit between model-predicted values and data. Within each MCMC run, we initialize CLiBeSO-W at 16 Myr ago and force the model with linear changes (both increases and decreases) in erosion over the late Cenozoic era. As a test against local minima, we run 5,000 distinct MCMC runs with perturbed initial parameters. Convergence typically occurs after 100 iterations of CLiBeSO-W. Owing to the turnover in $\delta^7\text{Li}_{\text{riv}}$ at moderate weathering intensities, the initial weathering intensity 16 Myr ago is a critical calibration point because of its effect on subsequent initial values of $\delta^7\text{Li}_{\text{riv}}$. We therefore test a wide range of initial weathering intensities (0.025–0.25) that span the maximum in $\delta^7\text{Li}_{\text{riv}}$ with weathering intensity. As a further test of whether decreasing inputs of carbon from volcanism can simultaneously explain the seawater $\delta^7\text{Li}$ and $^{10}\text{Be}/^9\text{Be}$ and the atmospheric p_{CO_2} records, we perform additional MCMC experiments in which only volcanism is permitted to decrease.

We estimate that the globally averaged silicate weathering intensity has declined by nearly 67% (full range: 46–80%) over the past 16 Myr (Fig. 1f). The mechanism that drives the underlying increase in land surface reactivity can be any process that exposes fresh, weakly

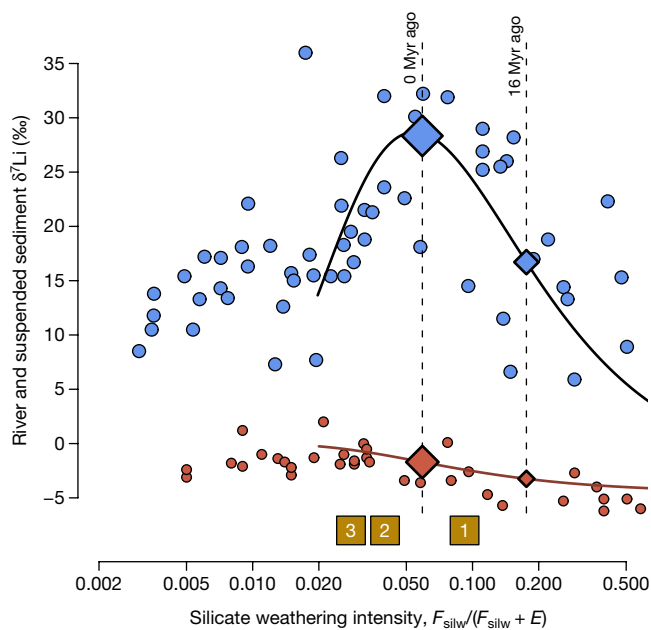


Fig. 2 | River and sediment $\delta^7\text{Li}$ as a function of silicate weathering intensity. The blue points are modern river $\delta^7\text{Li}$ data from ref. ²². The red points are suspended sediment $\delta^7\text{Li}$ from ref. ³¹. The black line is our model of $\delta^7\text{Li}_{\text{riv}}$ and the red line is our model of $\delta^7\text{Li}_{\text{sed}}$ as a function of weathering intensity. The brown squares are estimates of the global silicate weathering intensity calculated from independent estimates of denudation and the river dissolved silicate flux³³ (see Methods) (1: median soil production¹⁷; 2: river suspended sediment²³; and 3: cosmogenic ¹⁰Be denudation¹⁸). The diamonds are our estimate of global silicate weathering intensity and $\delta^7\text{Li}_{\text{riv}}$ (blue) and $\delta^7\text{Li}_{\text{sed}}$ (red) at 16 Myr ago (small) and 0 Myr ago (large).

weathered regolith—such as tectonic faulting and river incision driven by uplift, glacial reworking of the landscape, or faster removal of soil after a change in vegetation. However, regardless of the cause, to prevent regolith from returning to a state of high weathering intensity over the timescales investigated here, the land surface must be continuously eroded. This requirement is parameterized in equation (1), and consequently we find that the globally averaged erosion rate increases from around 16 m Myr⁻¹ at 16 Myr ago (full range: 11–23 m Myr⁻¹) to around 54 m Myr⁻¹ at 0 Myr ago (full range: 21–116 m Myr⁻¹) (Extended Data Fig. 1). We note that the absolute values of these increases in erosion rate are not of high confidence, as they depend upon the assumptions made in the parametrization of $\delta^7\text{Li}$. However, the conclusion of an increase in erosion is inescapable. The rate of increase determined here is similar to that of estimates based upon thermochronometry¹⁶ and sedimentary volumes¹⁵ (Fig. 1g), and we calculate a pre-anthropogenic erosion rate (0 Myr ago) that approximates, within uncertainty, independent estimates based upon suspended sediments¹⁵ and cosmogenic nuclides¹⁸.

As a consequence of decreasing weathering intensity, the atmospheric P_{CO_2} decreases from 517 p.p.m. in the mid-Miocene to a value of 263 p.p.m. in the late Quaternary period (full range: 244–300 p.p.m.) (Fig. 1b). The silicate weathering flux decreases by 6% (full range: -17% to +34%), whereas the carbonate weathering flux doubles (full range: 30%–340% increase) (Fig. 1e), which is consistent with an increase in the seawater ²⁶Mg/²⁴Mg ratio²⁹. Carbonate burial incorporates the alkalinity fluxes of both silicate and carbonate weathering, and thus increases by 51% (full range: 9%–180%), which matches estimates of the late Cenozoic increase from carbonate sedimentary volumes³⁰ (Fig. 1e). The estimates of carbonate weathering and burial are particularly uncertain because, when these processes are combined, they yield no long-term impact on the carbon cycle. We also predict that terrestrial pyrite oxidation fluxes more than triple (Extended Data Fig. 2), driven by greater erosion; however, this results in an increase in P_{CO_2}

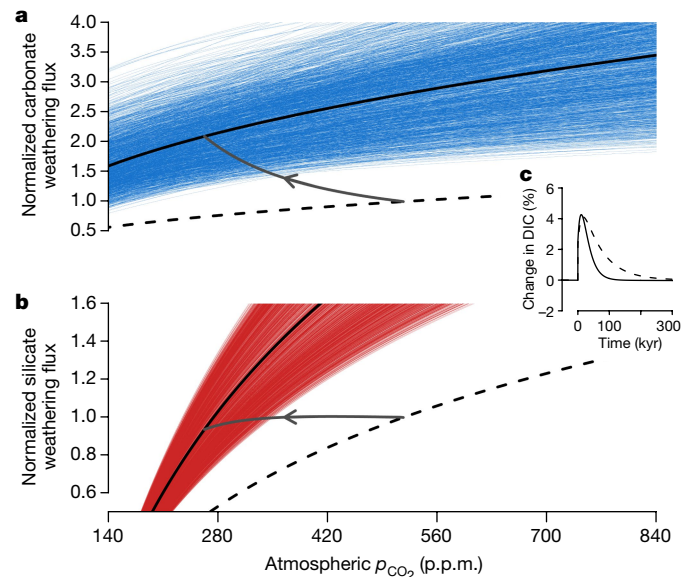


Fig. 3 | The functional form of the weathering feedback at 16 Myr ago and at 0 Myr ago. **a**, **b**, Carbonate (**a**) and silicate (**b**) weathering functional forms. The solid black lines are the functional form of the weathering feedback at 0 Myr ago; the thin coloured lines are the functional form for each convergent MCMC iteration. The solid black line uses the mean parameter values from the MCMC inversion. The dashed lines are the functional forms at 16 Myr ago. The grey arrows indicate the mean progression of carbonate and silicate weathering in the model as erosion increases. **c**, The response of total dissolved inorganic carbon (DIC) to an instantaneous 1,000 Pg C perturbation at both 0 Myr ago (solid line) and 16 Myr ago (dashed line), initialized with steady-state conditions for both time periods (see Methods). kyr, thousand years.

of only 6 p.p.m. relative to no change in pyrite oxidation fluxes. This suggests that, in contrast to the conclusions of a previous study¹², large, erosionally driven increases in pyrite oxidation have a minimal effect on the ocean–atmosphere carbon budget (Extended Data Fig. 3). This contradiction arises because, unlike in our model, the silicate weathering flux in the previous study¹² is calculated from the seawater ⁸⁷Sr/⁸⁶Sr record.

These results stem from the erosional forcing of silicate weathering. An increase in silicate weathering due to faster erosion removes CO₂. However, because silicate weathering is also responsive to climate (that is, P_{CO_2}), the consequently lower P_{CO_2} produces an approximately constant silicate weathering flux. Thus, the dependency of silicate weathering on erosion is non-stationary, with a greater erosion rate in the Quaternary required to produce the same silicate weathering flux as in the Miocene. The result is a decrease in the globally averaged silicate weathering intensity (Figs. 1f, 2).

It is notable that, with only a linear erosional forcing, modelled $\delta^7\text{Li}_{\text{oc}}$ initially increases but then begins to asymptote towards 0 Myr ago. This behaviour matches that of the $\delta^7\text{Li}$ record from foraminifera²⁸ (Figs. 1c, 2). Because $\delta^7\text{Li}_{\text{riv}}$ is maximized at a weathering intensity of approximately 0.05 (ref. ²²), an increase in erosion eventually results in a weathering intensity that is equal to or less than 0.05. Our estimate of modern global weathering intensity from $\delta^7\text{Li}$ broadly matches estimates of the global silicate weathering intensity from three independent methods (brown boxes in Fig. 2). Similarly, our estimate of the globally averaged suspended sediment $\delta^7\text{Li}$ value at 0 Myr ago matches data from a recent compilation³¹ (Fig. 2). A decrease in weathering intensity also results in declining lithium weathering fluxes, owing to the increasing partitioning of lithium into the clay fraction at moderate weathering intensities²² (Extended Data Fig. 4). Thus, we attribute constant foraminifera $\delta^7\text{Li}$ data during the Plio-Pleistocene²⁸ to increasing erosion that drove silicate weathering intensity towards the maximum weathering zone fractionation between bedrock and soil water $\delta^7\text{Li}$. Support for this hypothesis is provided by data that suggest a similar

late Cenozoic maximum in $^{11}\text{B}/^{10}\text{B}$ —a stable isotope system that, like $^7\text{Li}/^6\text{Li}$, also traces weathering intensity in the weathering zone due to the preferential incorporation of ^{10}B into clay minerals³².

In contrast to the results above, solely decreasing the fluxes of carbon from volcanism and the solid Earth fails to simultaneously match the late Cenozoic data of seawater $\delta^7\text{Li}$ and $^{10}\text{Be}/^9\text{Be}$ and of atmospheric P_{CO_2} (Extended Data Fig. 5). Alternatively, an increase in seawater $\delta^7\text{Li}$ could plausibly occur owing to an increase in weathering intensity if, 16 Myr ago, weathering intensity was lower than 0.05 (Fig. 2). However, decreases in erosion fail to match the atmospheric P_{CO_2} record, as an increase in weathering intensity results instead in an increase in atmospheric P_{CO_2} (Extended Data Fig. 6).

Our results point towards a coherent explanation for the climatic changes that occurred over the Neogene. The increase and plateau in seawater $\delta^7\text{Li}$ reflects a decline in silicate weathering intensity, and constant $^{10}\text{Be}/^9\text{Be}$ indicates constant silicate weathering fluxes. Variations in the partitioning of denudation with time between weathering and erosion provide a simple mechanism by which to explain P_{CO_2} changes without the need to invoke speculative, compensatory CO_2 fluxes. The result of a non-stationary weathering–erosion relationship is approximately constant global silicate weathering fluxes, even as erosion increases and P_{CO_2} declines. Therefore, these two isotopic systems combined reflect increasing land surface reactivity during the Neogene^{8,9}.

A consequence of a more reactive Earth surface is more efficient production of alkalinity, resulting in the same weathering flux at a lower P_{CO_2} . Further, a lower global weathering intensity suggests that there is a greater supply of unweathered minerals within the weathering zone with which to buffer a perturbation in the carbon cycle. The capacity of both carbonate and silicate weathering to respond to a carbon cycle perturbation in both the Miocene and the present is shown in Fig. 3, where we plot the normalized silicate and carbonate weathering fluxes against P_{CO_2} using the mid-Miocene and modern-day values for E and equation (1). The result of an increase in erosion is a greater capacity for weathering to respond to an increase in P_{CO_2} ; that is, a strengthened weathering feedback⁹. Consequently, the timescale for recovery of the ocean–atmosphere system to an instantaneous addition of carbon is 50% faster today than at 16 Myr ago (see Methods) (Fig. 3c). Thus, the Earth system today may be more buffered against perturbations in the carbon cycle than it was in the geologic past. This could potentially reduce the effects of, for example, CO_2 invasion on ocean chemistry compared to analogous perturbations in the Mesozoic and early Cenozoic eras.

Online content

Any Methods, including any statements of data availability and Nature Research reporting summaries, along with any additional references and Source Data files, are available in the online version of the paper at <https://doi.org/10.1038/s41586-019-1332-y>

Received: 22 November 2018; Accepted: 26 April 2019;
Published online 3 July 2019.

- Zachos, J., Pagani, M., Sloan, L., Thomas, E. & Billups, K. Trends, rhythms, and aberrations in global climate 65 Ma to present. *Science* **292**, 686–693 (2001).
- Herbert, T. D. et al. Late Miocene global cooling and the rise of modern ecosystems. *Nat. Geosci.* **9**, 843–847 (2016).
- Raymo, M. E. & Ruddiman, W. F. Tectonic forcing of late Cenozoic climate. *Nature* **359**, 117–122 (1992).
- Hay, W. W., Soeding, E., DeConto, R. M. & Wold, C. N. The late Cenozoic uplift—climate change paradox. *Int. J. Earth Sci.* **91**, 746–774 (2002).
- Sadler, P. M. Sediment accumulation rates and the completeness of stratigraphic sections. *J. Geol.* **89**, 569–584 (1981).
- Schildgen, T. F., van der Beek, P. A., Sinclair, H. D. & Thiede, R. C. Spatial correlation bias in late-Cenozoic erosion histories derived from thermochronology. *Nature* **559**, 89–93 (2018).
- Willenbring, J. K. & von Blanckenburg, F. Long-term stability of global erosion rates and weathering during late-Cenozoic cooling. *Nature* **465**, 211–214 (2010).
- Kump, L. R. & Arthur, M. A. in *Tectonic Uplift and Climate Change* (ed. Ruddiman, W. F.) 399–426 (Plenum Press, 1997).
- Caves, J. K., Jost, A. B., Lau, K. V. & Maher, K. Cenozoic carbon cycle imbalances and a variable silicate weathering feedback. *Earth Planet. Sci. Lett.* **450**, 152–163 (2016).

- Berner, R. A. & Caldeira, K. The need for mass balance and feedback in the geochemical carbon cycle. *Geology* **25**, 955–956 (1997).
- Raymo, M. E. in *Tectonic Uplift and Climate Change* (ed. Ruddiman, W. F.) 367–381 (Plenum Press, 1997).
- Torres, M. A., West, A. J. & Li, G. Sulphide oxidation and carbonate dissolution as a source of CO_2 over geological timescales. *Nature* **507**, 346–349 (2014).
- Li, G. & Elderfield, H. Evolution of carbon cycle over the past 100 million years. *Geochim. Cosmochim. Acta* **103**, 11–25 (2013).
- Zhang, P., Molnar, P. & Downs, W. R. Increased sedimentation rates and grain sizes 2–4 Myr ago due to the influence of climate change on erosion rates. *Nature* **410**, 891–897 (2001).
- Wilkinson, B. H. Humans as geologic agents: a deep-time perspective. *Geology* **33**, 161–164 (2005).
- Herman, F. et al. Worldwide acceleration of mountain erosion under a cooling climate. *Nature* **504**, 423–426 (2013).
- Dixon, J. L. & von Blanckenburg, F. Soils as pacemakers and limiters of global silicate weathering. *C. R. Geosci.* **344**, 597–609 (2012).
- Larsen, I. J., Montgomery, D. R. & Greenberg, H. M. The contribution of mountains to global denudation. *Geology* **42**, 527–530 (2014).
- Bataille, C. P., Willis, A., Yang, X. & Liu, X. Continental igneous rock composition: a major control of past global chemical weathering. *Sci. Adv.* **3**, e1602183 (2017).
- Berner, R. A. GEOCARBSULF: a combined model for Phanerozoic atmospheric O_2 and CO_2 . *Geochim. Cosmochim. Acta* **70**, 5653–5664 (2006).
- Bouchez, J., von Blanckenburg, F. & Schuessler, J. A. Modeling novel stable isotope ratios in the weathering zone. *Am. J. Sci.* **313**, 267–308 (2013).
- Dellinger, M. et al. Riverine Li isotope fractionation in the Amazon River basin controlled by the weathering regimes. *Geochim. Cosmochim. Acta* **164**, 71–93 (2015).
- von Blanckenburg, F. & Bouchez, J. River fluxes to the sea from the ocean's $^{10}\text{Be}/^9\text{Be}$ ratio. *Earth Planet. Sci. Lett.* **387**, 34–43 (2014).
- Shields, G. A. & Mills, B. J. W. Tectonic controls on the long-term carbon isotope mass balance. *Proc. Natl Acad. Sci. USA* **114**, 4318–4323 (2017).
- Myhre, G., Highwood, E. J., Shine, K. P. & Stordal, F. New estimates of radiative forcing due to well mixed greenhouse gases. *Geophys. Res. Lett.* **25**, 2715–2718 (1998).
- von Blanckenburg, F., Bouchez, J. & Wittmann, H. Earth surface erosion and weathering from the $^{10}\text{Be}(\text{meteoric})/^9\text{Be}$ ratio. *Earth Planet. Sci. Lett.* **351–352**, 295–305 (2012).
- Dellinger, M. et al. Lithium isotopes in large rivers reveal the cannibalistic nature of modern continental weathering and erosion. *Earth Planet. Sci. Lett.* **401**, 359–372 (2014).
- Misra, S. & Froelich, P. N. Lithium isotope history of Cenozoic seawater: changes in silicate weathering and reverse weathering. *Science* **335**, 818–823 (2012).
- Pogge von Strandmann, P. E., Forshaw, J. & Schmidt, D. N. Modern and Cenozoic records of seawater magnesium from foraminiferal Mg isotopes. *Biogeosciences* **11**, 5155–5168 (2014).
- Opdyke, B. N. & Wilkinson, B. H. Surface area control of shallow cratonic to deep marine carbonate accumulation. *Paleoceanography* **3**, 685–703 (1988).
- Dellinger, M., Bouchez, J., Gaillardet, J., Faure, L. & Moureau, J. Tracing weathering regimes using the lithium isotope composition of detrital sediments. *Geology* **45**, 411–414 (2017).
- Greenop, R. et al. A record of Neogene seawater $\delta^{11}\text{B}$ reconstructed from paired $\delta^{11}\text{B}$ analyses on benthic and planktic foraminifera. *Clim. Past* **13**, 149–170 (2017).
- Gaillardet, J., Dupré, B., Louvat, P. & Allegre, C. Global silicate weathering and CO_2 consumption rates deduced from the chemistry of large rivers. *Chem. Geol.* **159**, 3–30 (1999).

Acknowledgements We thank S. Gallen, K. Lau, K. Maher, D. Stolper, S. Willett and M. Winnick for discussions regarding erosion, weathering and lithium isotopes. J.K.C.R. is funded by an ETH Fellowship. D.E.I. is supported by the Heising-Simons Foundation.

Reviewer information Nature thanks Darryl Granger, Lee Kump and the other anonymous reviewer(s) for their contribution to the peer review of this work.

Author contributions All authors developed the scientific concept. J.K.C.R. developed the model, conducted the analysis, and led the writing of the manuscript. All authors provided input on the manuscript.

Competing interests The authors declare no competing interests.

Additional information

Extended data is available for this paper at <https://doi.org/10.1038/s41586-019-1332-y>.

Supplementary information is available for this paper at <https://doi.org/10.1038/s41586-019-1332-y>.

Reprints and permissions information is available at <http://www.nature.com/reprints>.

Correspondence and requests for materials should be addressed to J.K.C.R.

Publisher's note: Springer Nature remains neutral with regard to jurisdictional claims in published maps and institutional affiliations.

© The Author(s), under exclusive licence to Springer Nature Limited 2019

METHODS

CLiBeSO-W model equations. We develop a carbon cycle model that tracks Li and Be to quantify how changes in erosion affect weathering and climate. CLiBeSO-W is adapted from and is a simplified version of the COPSE and GEOCARB models^{20,24,34}. The mass balance forward model solves for the time-varying reservoirs of carbon (C) and alkalinity (A) as a function of the major fluxes of C and A to and from the ocean–atmosphere system, according to equations (4) and (5):

$$\frac{dC}{dt} = F_{\text{carb,w}} + F_{\text{org,w}} + F_{\text{volc}} - F_{\text{carb,b}} - F_{\text{org,b}} + F_{\text{sulf,w}} - F_{\text{sulf,b}} \quad (4)$$

and

$$\frac{dA}{dt} = 2F_{\text{carb,w}} + 2F_{\text{sil,w}} - 2F_{\text{carb,b}} \quad (5)$$

where $F_{\text{carb,w}}$, $F_{\text{org,w}}$ and $F_{\text{sil,w}}$ are the carbonate, organic and silicate weathering fluxes, respectively, F_{volc} is the volcanic flux, and $F_{\text{carb,b}}$ and $F_{\text{org,b}}$ are the carbonate and organic burial fluxes (mol C yr⁻¹). We discuss $F_{\text{sulf,w}}$ and $F_{\text{sulf,b}}$ (mol C yr⁻¹)—the fluxes of carbon due to the oxidative weathering and burial, respectively, of pyrite—under the section ‘Coupled sulfur–carbon cycle’.

We follow ref. ⁹ in parameterizing $F_{\text{sil,w}}$ as a function of climate and of Earth surface reactivity:

$$F_{\text{sil,w}} = k(\log_2(R_{\text{CO}_2}) + 1) \quad (6)$$

where R_{CO_2} is the ratio of P_{CO_2} at time t to pre-industrial values (280 p.p.m.), \log_2 describes the sensitivity of the Earth system to P_{CO_2} (refs ^{25,35,36}), and k (mol C yr⁻¹) is a constant of proportionality that encapsulates the reactivity of the Earth surface (modified by, for example, vegetation, erosion, lithology and exposed continental area) and translates the effect of climate into $F_{\text{sil,w}}$. Notably, when $R_{\text{CO}_2} = 1$, $k = F_{\text{sil,w}}$. Because we are interested in quantifying how changes in erosion (E) effect changes in $F_{\text{sil,w}}$, we factor a non-dimensional erosion term out of k :

$$F_{\text{sil,w}} = \left(\frac{E}{E_0}\right)^{\alpha_{\text{sil}}} k_1(\log_2(R_{\text{CO}_2}) + 1) \quad (7)$$

where α_{sil} permits a nonlinear response of $F_{\text{sil,w}}$ to changes in erosion, k_1 is assumed to remain constant through the late Cenozoic, and E_0 (metric tonnes per year, t yr⁻¹) is the initial erosion at 16 Myr ago. In this formulation, $\left(\frac{E}{E_0}\right)^{\alpha_{\text{sil}}} k_1$ represents the reactivity of the Earth surface as modified by erosion (E) and k_1 , which encapsulates the remaining parameters that modify reactivity, such as lithology. Because we assume that k_1 is constant over the Neogene, any reactivity changes are due to a change in E . Erosion can sustain a prolonged change in reactivity by constantly rejuvenating regolith that would otherwise obtain a high weathering intensity (WI). Equation (7) further encapsulates the silicate weathering feedback: to balance constant long-term carbon input fluxes, changes in the $(\log_2(R_{\text{CO}_2}) + 1)$ term of the equation must be matched by simultaneous changes in the $\left(\frac{E}{E_0}\right)^{\alpha_{\text{sil}}} k_1$ term.

We parameterize $F_{\text{carb,w}}$ following ref. ²⁴ as a function of temperature (T)—instead of R_{CO_2} —although these two formulations have similar functional forms (Fig. 3) and both T and R_{CO_2} represent the climatic dependence on weathering.

$$F_{\text{carb,w}} = k_{\text{carb}} \left(\frac{E}{E_0}\right)^{\alpha_{\text{carb}}} e^{(0.05(T-288))} \quad (8)$$

where k_{carb} (mol C yr⁻¹) is a constant of proportionality that represents the Earth surface carbonate reactivity, and α_{carb} modulates the sensitivity of $F_{\text{carb,w}}$ to changes in E . We calculate T as a function of P_{CO_2} assuming an Earth system climate sensitivity that ranges from 3 °C to 9 °C per CO₂ doubling^{35–37}. When $E/E_0 = 1$ and $T = 288$, $k_{\text{carb}} = F_{\text{carb,w}}$. Similar to $F_{\text{sil,w}}$, $F_{\text{carb,w}}$ increases due to changes in E , although cooling results in a slightly lower $F_{\text{carb,w}}$ than would be expected if it were solely influenced by changes in E . Because changes in $F_{\text{carb,w}}$ are balanced by changes in $F_{\text{carb,b}}$, increasing $F_{\text{carb,w}}$ has no long-term effect on P_{CO_2} . $F_{\text{org,w}}$ is parameterized only as a function of E , given evidence that oxidation of petrogenic organic carbon is tightly linked to erosion^{24,38,39}:

$$F_{\text{org,w}} = F_{\text{org,w},0} \left(\frac{E}{E_0}\right)^{\alpha_{\text{orgw}}} \quad (9)$$

where $F_{\text{org,w},0}$ is the initial flux of CO₂ due to oxidation of geologic organic carbon. As with $F_{\text{sil,w}}$ and $F_{\text{carb,w}}$, α_{orgw} is an exponent that modulates the sensitivity of $F_{\text{org,w}}$ to changes in E .

Following previous carbon cycle models^{40,41}, we treat $F_{\text{carb,b}}$ as a function of the ratio of the seawater carbonate saturation state (Ω) at time t to Ω at the start of the model run ($t = 0$):

$$F_{\text{carb,b}} = F_{\text{carb,b},0} \left(\frac{\Omega_t}{\Omega_0}\right) \quad (10)$$

where $F_{\text{carb,b},0}$ is the initial carbonate burial flux, and

$$\Omega = \frac{[\text{Ca}^{2+}][\text{CO}_3^{2-}]}{K_{\text{sp}}} \quad (11)$$

where K_{sp} is the solubility product of calcite⁴² and $[\text{Ca}^{2+}]$ is assumed equal to that of modern seawater. We do not correct for changes in seawater $[\text{Ca}^{2+}]$ or $[\text{Mg}^{2+}]$ during the late Cenozoic⁴³.

Given increasing evidence for an erosional control on terrestrial organic carbon burial^{20,38,44–46}, we parameterize $F_{\text{org,b}}$ as a function of both E and carbonate burial:

$$F_{\text{org,b}} = F_{\text{org,b},0} \left(\frac{E}{E_0}\right)^{\alpha_{\text{orgb}}} \left(\frac{F_{\text{carb,b}}}{F_{\text{carb,b},0}}\right) \quad (12)$$

where $F_{\text{org,b},0}$ is the initial organic carbon burial flux, and α_{orgb} describes the dependency of $F_{\text{org,b}}$ on E . The dependency on carbonate burial suggests that the rain ratio (that is, the ratio between organic carbon and carbonate carbon export to ocean sediments) has been constant during the late Cenozoic⁴⁷. We test the effect of this $F_{\text{org,b}}$ parameterization by testing an alternative parameterization that includes a phosphorus (P) sub-cycle that links $F_{\text{org,b}}$ with phosphorus supply^{24,46}:

$$F_{\text{org,b}} = F_{\text{org,b},0} \left(\frac{E}{E_0}\right)^{\alpha_{\text{orgb}}} \left(\frac{[\text{P}]_{\text{oc}}}{[\text{P}]_{\text{oc},0}}\right)^2 \quad (13)$$

where $[\text{P}]_{\text{oc}}$ is the concentration of P in seawater and $[\text{P}]_{\text{oc},0}$ is the initial concentration at 16 Myr ago (2.21 μmol P l⁻¹) (ref. ⁴⁸). The weathering of carbonate, silicate and organic carbon-bearing rock^{24,46,48,49} supplies P to the ocean (after ref. ⁴⁶):

$$F_{\text{pw}} = F_{\text{pw},0} \left[k_{\text{sil,p}} \left(\frac{F_{\text{sil,w}}}{F_{\text{sil,w},0}}\right) + k_{\text{carb,p}} \left(\frac{F_{\text{carb,w}}}{F_{\text{carb,w},0}}\right) + k_{\text{orgw,p}} \left(\frac{F_{\text{orgw}}}{F_{\text{orgw},0}}\right) \right] \quad (14)$$

where $F_{\text{pw},0}$ is the initial weathering flux of P (47 Gmol yr⁻¹), and k_i is the fraction of P derived from silicate ($i = \text{sil,p}$), carbonate ($i = \text{carb,p}$) or organic carbon ($i = \text{orgw,p}$) weathering. Following refs ^{24,46}, we treat P as being primarily supplied by the weathering of silicates ($k_{\text{sil,p}} = 0.58$; $k_{\text{carb,p}} = 0.21$; $k_{\text{orgw,p}} = 0.21$). Burial of P in the marine environment is a first-order reaction dependent upon $[\text{P}]_{\text{oc}}$ (refs ^{48,49}):

$$F_{\text{pb}} = F_{\text{pb},0} \left(\frac{[\text{P}]_{\text{oc}}}{[\text{P}]_{\text{oc},0}}\right) \quad (15)$$

where $F_{\text{pb},0}$ is the initial flux of buried P, set equal to $F_{\text{pw},0}$, such that the phosphorus cycle starts in steady-state.

With $F_{\text{org,b}}$ linked to $[\text{P}]_{\text{oc}}$, we predict an erosion flux at 0 Myr ago of 45 m Myr⁻¹ (full range: 22–82 m Myr⁻¹), compared with 54 m Myr⁻¹ in Fig. 1, and P_{CO_2} at 0 Myr ago of 274 p.p.m., which is 12 p.p.m. higher than in Fig. 1. Consequently, our primary conclusions are relatively insensitive to our parameterization of $F_{\text{org,b}}$. **Coupled sulfur–carbon cycle.** We include a simple parameterization of the long-term sulfur cycle and its effect on the carbon cycle. We do this by including terms that modify the total reservoir of carbon as a function of oxidative pyrite weathering ($F_{\text{sulf,w}}$) and of sulfur reduction and pyrite formation on the sea floor ($F_{\text{sulf,b}}$). Inclusion of the pyrite fluxes in the carbon mass balance (equation (4)) suggests that the H⁺ liberated owing to pyrite oxidation is primarily used to chemically weather co-occurring carbonate minerals, which releases bicarbonate.

$F_{\text{sulf,w}}$ is parameterized as a linear function of E , given evidence that pyrite oxidation fluxes are modulated by the supply of material to the weathering zone^{50–52}:

$$F_{\text{sulf,w}} = F_{\text{sulf,w},0} \left(\frac{E}{E_0}\right)^{\alpha_{\text{sulf}}} \quad (16)$$

where $F_{\text{sulf,w},0}$ is the initial pyrite oxidation flux (mol S yr⁻¹) at 16 Myr ago and $\alpha_{\text{sulf}} = 1$ under the assumption that pyrite oxidation is always supply-limited. This flux is converted to an equivalent carbon flux, assuming that pyrite oxidation results in the release of two moles of CO₂ per oxidized mole of pyrite⁵³. We set $F_{\text{sulf,w},0}$ to 500 Gmol yr⁻¹ such that the estimated increase in erosion produces an $F_{\text{sulf,w}}$ at 0 Myr ago (1,700 Gmol yr⁻¹) that matches recent estimates of the modern global pyrite weathering flux⁵⁴.

Sulfur reduction and pyrite burial on the sea floor (F_{sulfb}) is parameterized as a first-order reaction dependent upon the burial of organic matter^{34,55}:

$$F_{\text{sulfb}} = F_{\text{sulfb},0} \left(\frac{F_{\text{orgb}}}{F_{\text{orgb},0}} \right) \quad (17)$$

where $F_{\text{sulfb},0}$ is the initial pyrite burial flux. As with pyrite oxidation (equation (16)), we assume that sulfur reduction consumes two moles of CO_2 per mole of reduced sulfur¹².

Although our parameterization of the redox fluxes (sulfur and organic carbon cycles) are simplified, CLiBeSO-W is insensitive to the inclusion of these fluxes. Exclusion of the redox fluxes results in an erosional flux at 0 Myr ago of 61 m Myr^{-1} (full range: 34–101 m Myr^{-1}) and P_{CO_2} at 0 Myr ago of 257 p.p.m., similar to our estimates in Fig. 1.

Modelled $^{10}\text{Be}/^9\text{Be}$. The $^{10}\text{Be}/^9\text{Be}$ of the ocean is set by the ratio of the downward flux of meteoric ^{10}Be (F_{met} , in atoms $\text{Be km}^{-2} \text{yr}^{-1}$), produced in the atmosphere owing to cosmic ray bombardment) to the upward exhumation flux of ^9Be that is released by weathering into the weathering zone^{23,26}:

$$\frac{^{10}\text{Be}}{^9\text{Be}} = \frac{R_{\text{area}} F_{\text{met}} + \varphi_{\text{del}} F_{\text{met}}}{\varphi_{\text{del}} F_{\text{silw}} [\text{Be}]_{\text{rock}}} \quad (18)$$

where R_{area} is the ratio of the area of ocean to land, φ_{del} is the fraction of Be that is ultimately delivered to the ocean by rivers, $[\text{Be}]_{\text{rock}}$ is the average concentration of Be (in p.p.m.) in silicate bedrock subject to weathering, and F_{silw} is the silicate weathering flux. Here in equation (18), F_{silw} has units of t yr^{-1} . We describe the conversion between mol C yr^{-1} and t yr^{-1} in the section ‘Calculating F_{silw} , E , and WI ’ below.

Equation (18) differs somewhat from the equation originally presented in ref. 23:

$$\frac{^{10}\text{Be}}{^9\text{Be}} = \frac{R_{\text{area}} F_{\text{met}} + \varphi_{\text{del}} F_{\text{met}}}{\varphi_{\text{del}} D [\text{Be}]_{\text{rock}} f_{\text{reac}}} \quad (19)$$

where D is total denudation ($F_{\text{silw}} + E$) and f_{reac} is the fraction of Be released during solubilization of the bedrock (that is, the fraction of Be released from primary minerals during weathering). In equating F_{silw} and $D \times f_{\text{reac}}$, we are assuming that the silicate weathering flux is proportional to the solubilization flux of ^9Be (ref. 56). Lastly, because the residence time of Be in the ocean is short ($< 1,000$ years)²³, we assume a steady state in the marine beryllium cycle.

We are interested in parameterizing how changes in erosion drive changes in global F_{silw} rather than predicting basin-scale differences in F_{silw} ; therefore, we normalize the $^{10}\text{Be}/^9\text{Be}$ data to the current $^{10}\text{Be}/^9\text{Be}$ ratio of the respective ocean basin. For the model-predicted $^{10}\text{Be}/^9\text{Be}$, we normalize the model $^{10}\text{Be}/^9\text{Be}$ to the $^{10}\text{Be}/^9\text{Be}$ at 0 Myr ago ($(^{10}\text{Be}/^9\text{Be})_0$), under the assumption that, over the late Neogene, the main parameters (φ_{del} , R_{area} and F_{met}) in equation (18) have remained approximately constant. This enables us to eliminate φ_{del} , R_{area} , and F_{met} . Consequently, equation (18) becomes

$$\frac{\frac{^{10}\text{Be}}{^9\text{Be}}}{\left(\frac{^{10}\text{Be}}{^9\text{Be}} \right)_0} = \frac{F_{\text{silw},0}}{F_{\text{silw}}} \quad (20)$$

where $F_{\text{silw},0}$ is the silicate weathering flux at 0 Myr ago. Although we realize that the assumption that φ_{del} , R_{area} , and F_{met} have been constant over the Neogene is restrictive, it is difficult to quantify any changes over time. The use of a constant φ_{del} is justified as there are three different delivery pathways of ^9Be through the coastal trap that are probably independent of sediment flux^{23,57}. R_{area} has declined over the Neogene as the eustatic sea level has fallen, although the magnitude of the fall in sea level is disputed^{58,59}. Lastly, our results are insensitive to the inclusion of carbonate-sourced Be, even though carbonate rocks have a low average concentration²⁶ of 0.6 p.p.m. Be. Including the flux of carbonate-sourced Be results in an erosion flux at 0 Myr ago of 49 m Myr^{-1} (full range: 26–81 m Myr^{-1}) and an estimated P_{CO_2} at 0 Myr ago of 265 p.p.m., which are similar to our estimates in Fig. 1.

Modelled $\delta^7\text{Li}$. We develop a mechanistic model of Li in the weathering zone to calculate both $\delta^7\text{Li}$ and the Li flux. Li isotopes and the Li flux are both nonlinearly dependent on the silicate $\text{WI}^{21,22,60}$. We follow ref. 21 in modelling riverine $\delta^7\text{Li}$ ($\delta^7\text{Li}_{\text{riv}}$):

$$\delta^7\text{Li}_{\text{riv}} = - \frac{E^{\text{Li}}}{W^{\text{Li}}} (\delta^7\text{Li}_{\text{sed}} - \delta^7\text{Li}_{\text{rock}}) + \delta^7\text{Li}_{\text{rock}} \quad (21)$$

where E^{Li} and W^{Li} (t yr^{-1}) are the erosion and weathering fluxes of Li, respectively. To convert to WI, we note that

$$\frac{E^{\text{Li}}}{W^{\text{Li}}} = \frac{(1 - \text{WI}^{\text{Li}})}{\text{WI}^{\text{Li}}} \quad (22)$$

where WI^{Li} is the dimensionless Li-specific WI. We assume that WI^{Li} is equivalent to silicate WI and hence that $E^{\text{Li}}/W^{\text{Li}}$ equals E/F_{silw} . This assumption is not strictly true, but we show in Fig. 2 that this assumption provides a reasonable fit to observed $\delta^7\text{Li}_{\text{riv}}$ data. However, we note that this may introduce a bias in our estimates of global silicate WI compared with independent estimates of global WI. We explain how we calculate WI from E and F_{silw} in the section ‘Calculating F_{silw} , E , and WI ’ below.

Sedimentary $\delta^7\text{Li}$ ($\delta^7\text{Li}_{\text{sed}}$) is also dependent upon WI^{31} with a relationship that resembles a negative exponential (see Fig. 3 in ref. 31):

$$\delta^7\text{Li}_{\text{sed}} = a e^{-\frac{b}{\text{WI}}} + \delta^7\text{Li}_{\text{rock}} \quad (23)$$

where a and b are constants (Extended Data Table 1) fit to the data of ref. 31, assuming that, at low WI, $\delta^7\text{Li}_{\text{sed}}$ is dominated by the transport of primary minerals rather than fine-grained reaction products (that is, clays). Substituting equations (22) and (23) into equation (21), we obtain:

$$\delta^7\text{Li}_{\text{riv}} = - \frac{(1 - \text{WI})}{\text{WI}} \left(a e^{-\frac{b}{\text{WI}}} \right) + \delta^7\text{Li}_{\text{rock}} \quad (24)$$

In Fig. 2 we plot our predicted $\delta^7\text{Li}_{\text{riv}}$ against the data from ref. 22. Except for very low WI ($\text{WI} < 0.02$), equation (24) captures both the highest measured $\delta^7\text{Li}_{\text{riv}}$ at $\text{WI} \approx 0.05$ and the reversal in apparent ^7Li fractionation as a function of WI.

The Li flux is also sensitive to WI (ref. 22). At high WI, most Li is partitioned into the dissolved load; however, at low WI, Li becomes increasingly incorporated into secondary clay minerals²¹. Ref. 22 demonstrated that the fraction of Li incorporated into clays is related to $\delta^7\text{Li}_{\text{riv}}$ via a Rayleigh distillation function.

$$\delta^7\text{Li}_{\text{riv}} = \delta^7\text{Li}_{\text{rock}} + \Delta_{\text{sec}} \log(f) \quad (25)$$

where Δ_{sec} is the ^7Li fractionation between water and secondary minerals and f is the fraction of Li partitioned from the bedrock into the dissolved load. To calculate the Li flux, we take advantage of the fact that we independently calculate $\delta^7\text{Li}_{\text{riv}}$ and solve equation (25) for f . We then use f to relate the Li flux to F_{silw} :

$$F_{w,\text{Li}} = F_{w,\text{Li},0} \left(\frac{F_{\text{silw}}}{F_{\text{silw},0}} \right) [1 + (f - f_0)] \quad (26)$$

where $F_{w,\text{Li},0}$ is the initial Li weathering flux (mol Li yr^{-1}) at 16 Myr ago, and f_0 is the initial fraction of Li partitioned into the dissolved load at 16 Myr ago. We assume that $\Delta_{\text{sec}} = -17\%$ (ref. 22) and is constant over the Neogene. Equation (26) permits the Li weathering flux to be coupled to both the global silicate weathering flux as well as the WI.

Seawater lithium model. To calculate seawater $\delta^7\text{Li}$ ($\delta^7\text{Li}_{\text{oc}}$), we embed a Li-isotope box-model within our carbon cycle model that includes the four major Li fluxes that impact the oceanic Li reservoir (M_{Li}) (refs 28,61):

$$\frac{dM_{\text{Li}}}{dt} = F_{w,\text{Li}} + F_{h,\text{Li}} - F_{\text{ba},\text{Li}} - F_{\text{rw},\text{Li}} \quad (27)$$

where $F_{h,\text{Li}}$ is the flux of Li from submarine hydrothermal vents, $F_{\text{ba},\text{Li}}$ is the flux of Li removed by alteration of sea-floor basalts, and $F_{\text{rw},\text{Li}}$ is the flux of Li removed by incorporation into sea-floor clays (mol Li yr^{-1}) (Extended Data Table 1). We parameterize the removal fluxes ($F_{\text{ba},\text{Li}}$ and $F_{\text{rw},\text{Li}}$) as first-order reactions dependent upon the concentration of Li in seawater ($[\text{Li}]_{\text{oc}}$):

$$F_{\text{ba},\text{Li}} = F_{\text{ba},\text{Li},0} \left(\frac{[\text{Li}]_{\text{oc}}}{[\text{Li}]_{\text{oc},0}} \right) \quad (28)$$

and

$$F_{\text{rw},\text{Li}} = F_{\text{rw},\text{Li},0} \left(\frac{[\text{Li}]_{\text{oc}}}{[\text{Li}]_{\text{oc},0}} \right) \quad (29)$$

where $F_{\text{ba},\text{Li},0}$ and $F_{\text{rw},\text{Li},0}$ are the initial fluxes of $F_{\text{ba},\text{Li}}$ and $F_{\text{rw},\text{Li}}$, respectively, and $[\text{Li}]_{\text{oc},0}$ is the initial concentration of Li in seawater (mol l^{-1}). Similarly, the hydrothermal flux of Li ($F_{h,\text{Li}}$) is proportional to F_{volc} :

$$F_{h,\text{Li}} = F_{h,\text{Li},0} \left(\frac{F_{\text{volc}}}{F_{\text{volc},0}} \right) \quad (30)$$

where $F_{h, Li, 0}$ is the initial hydrothermal Li flux, $F_{volc, 0}$ is the initial carbon flux from volcanism and solid Earth degassing, and F_{volc} is the volcanism and solid Earth carbon flux at time t . Note that in the main text results, F_{volc} is constant and equals $F_{volc, 0}$ through the Neogene. Because ${}^6\text{Li}$ is approximately 8% as abundant as ${}^7\text{Li}$ (ref. ⁶²), we use the full equation for the mass balance of this isotopic system as modified from refs ^{63,64}:

$$\frac{d(r_{oc})}{dt} = \left[\frac{1}{M_{Li}} \right] \left[F_{w, Li}(r_{riv} - r_{oc}) \left(\frac{1+r_{oc}}{1+r_{riv}} \right) + F_{h, Li}(r_h - r_{oc}) \left(\frac{1+r_{oc}}{1+r_h} \right) - F_{ba, Li} \varepsilon_{ba} \left(\frac{1+r_{oc}}{1+\varepsilon_{ba}+r_{oc}} \right) - F_{rw, Li} \varepsilon_{rw} \left(\frac{1+r_{oc}}{1+\varepsilon_{rw}+r_{oc}} \right) \right] \quad (31)$$

where r_i is the ${}^7\text{Li}/{}^6\text{Li}$ ratio of seawater ($i = oc$), rivers ($i = riv$) or of the hydrothermal flux ($i = h$), ε_{ba} is the ${}^7\text{Li}$ fractionation associated with the incorporation of Li into basalts and ε_{rw} is the ${}^7\text{Li}$ fractionation associated with the incorporation of Li into clays⁶¹, which is assumed to be equal to Δ_{sec} (Extended Data Table 1). The extra fractional terms in equation (31) $[(1+r_{oc})/(1+r_i)]$ account for the non-negligible contribution of ${}^6\text{Li}$ to the total concentration of Li (ref. ⁶⁴).

Model initial conditions, Monte Carlo routine and data constraints. We start the carbon, sulfur and lithium cycles at flux and isotopic steady state with the initial conditions listed in Extended Data Table 1. In brief, we assume an atmospheric P_{CO_2} and pH at 16 Myr ago of 517 p.p.m. (refs ⁶⁵⁻⁶⁷) and 8, respectively, and a globally averaged surface temperature of 15 °C. We force the model with changes in erosion (increases and decreases) and use a MCMC to optimize the fit between the model estimated values and the observed values of atmospheric P_{CO_2} (refs ⁶⁵⁻⁸¹), $\delta^7\text{Li}_{oc}$ (ref. ²⁸) and $({}^{10}\text{Be}/{}^9\text{Be})_{oc}$ (ref. ⁷). The model results are largely insensitive to the inclusion of the ${}^{10}\text{Be}/{}^9\text{Be}$ weathering proxy. MCMC simulations that exclude ${}^{10}\text{Be}/{}^9\text{Be}$ data provide nearly identical evolution of all fluxes and P_{CO_2} , although F_{silw} and E are less well constrained. The full range of F_{silw} changes that are permissible with our inversion scheme when excluding ${}^{10}\text{Be}/{}^9\text{Be}$ data cover a wide range from -47% to +179%, even though the mean results are nearly unchanged (Extended Data Fig. 7). Because many of the initial parameters are unknown, we vary these parameters for each of the 5,000 MCMC runs (see Extended Data Table 1). Convergence typically occurs after 100 iterations, and we iterate 300 times before using the final, optimized values. We use the 'Isodes' function in the deSolve package⁸² in R to solve stiff ODE systems, a time-step of 0.1 Myr due to the small forcing applied at each time step, and the carbonate constants presented in ref. ⁴².

Because we do not know precisely the initial values for many of the parameters in the equations above, each MCMC run uses perturbed parameters so as to preclude local minima in our estimate of the change in E required to explain the data. Notably, we use a wide range of initial WI, which is critical for estimating the evolution of $\delta^7\text{Li}_{oc}$, given the turnover in $\delta^7\text{Li}_{riv}$ at moderate WI. The initial WI determines the initial $\delta^7\text{Li}_{riv}$ and $\delta^7\text{Li}_{sed}$ values (equations (23) and (24)) and the subsequent evolution of $\delta^7\text{Li}_{riv}$. Because we force the Li sub-cycle to be in isotopic steady state at 16 Myr ago, we vary ε_{ba} to ensure Li isotope steady state at 16 Myr ago, as the value of ε_{ba} is poorly known⁶¹. Many of the models never converge to match the seawater $\delta^7\text{Li}$ and ${}^{10}\text{Be}/{}^9\text{Be}$ and atmospheric P_{CO_2} records, suggesting that some combinations of the parameters are implausible.

Calculating F_{silw} , E , and WI. To calculate seawater ${}^{10}\text{Be}/{}^9\text{Be}$ and $\delta^7\text{Li}_{riv}$, the silicate weathering flux (F_{silw}) is parameterized as a flux with units of t yr^{-1} . Ref. ³³ calculated a global net CO_2 consumption flux of $4,350 \text{ Gmol yr}^{-1}$ and global silicate total dissolved solids of 550 Mt yr^{-1} , and we use this ratio to convert between mol C and tonnes.

To calculate WI, we must also calculate a dimensional E (t yr^{-1}). To do so, we assume that the global ratio of E to F_{silw} at 16 Myr ago ranges between 3 and 40 (ref. ²¹). Consequently, an initial global E at 16 Myr ago can be calculated by converting F_{silw} into tonnes per year and then multiplying by the assumed ratio $E:F_{silw}$. At 0 Myr ago, we calculate an $E:F_{silw}$ of 17 using the mean of the optimized parameters (full range: 7–30). This corresponds to an estimated global E of 13 Gt yr^{-1} (full range: 5–27 Gt yr^{-1}), which is similar to the estimated non-anthropogenic, exorheic erosion flux ($10\text{--}19 \text{ Gt yr}^{-1}$) (refs ^{15,18,83-85}). For comparison between our estimate and data in Fig. 1g, we convert these and our model estimated erosion fluxes into an erosion rate (m Myr^{-1}), assuming a rock density of 2.8 g cm^{-3} and an exorheic area of $84.3 \text{ million km}^2$. We also calculate modern-day global WI using the global dissolved silicate flux³³ and three independent methods of estimating denudation as a comparison with our model-based estimate (points 1, 2, and 3 in Fig. 2): median soil production rate¹⁷, erosion derived from river suspended sediment^{23,85}; and cosmogenic ${}^{10}\text{Be}$ estimates of denudation¹⁸.

Calculating the recovery timescale for a carbon cycle perturbation. We compare the response of the middle Miocene (16 Myr ago) and modern (0 Myr ago) weathering fluxes and carbon cycle to a sudden injection of $1,000 \text{ Pg C}$ (Fig. 3).

First, for the 16-Myr-ago scenario, we use our initial conditions as outlined above, which are at steady state. To test the 0-Myr-ago case, we permit the CLiBeSO-W model to reach a steady state with the estimated increase in erosion over the late Cenozoic. Second, for each time period, we run the CLiBeSO-W model for 2 Myr with a 100-year time step. At 100,000 years after model initiation, we instantaneously inject an additional $1,000 \text{ Pg C}$ by adding it to the volcanic flux. Because the CLiBeSO-W model does not differentiate between atmosphere and ocean, this is equivalent to injecting $1,000 \text{ Pg C}$ into the dissolved inorganic carbon pool. We calculate the recovery timescale as the time required for approximately 63% ($1 - 1/e$; that is, the e -folding timescale) of the additional C to be removed from the total dissolved inorganic carbon.

Data availability

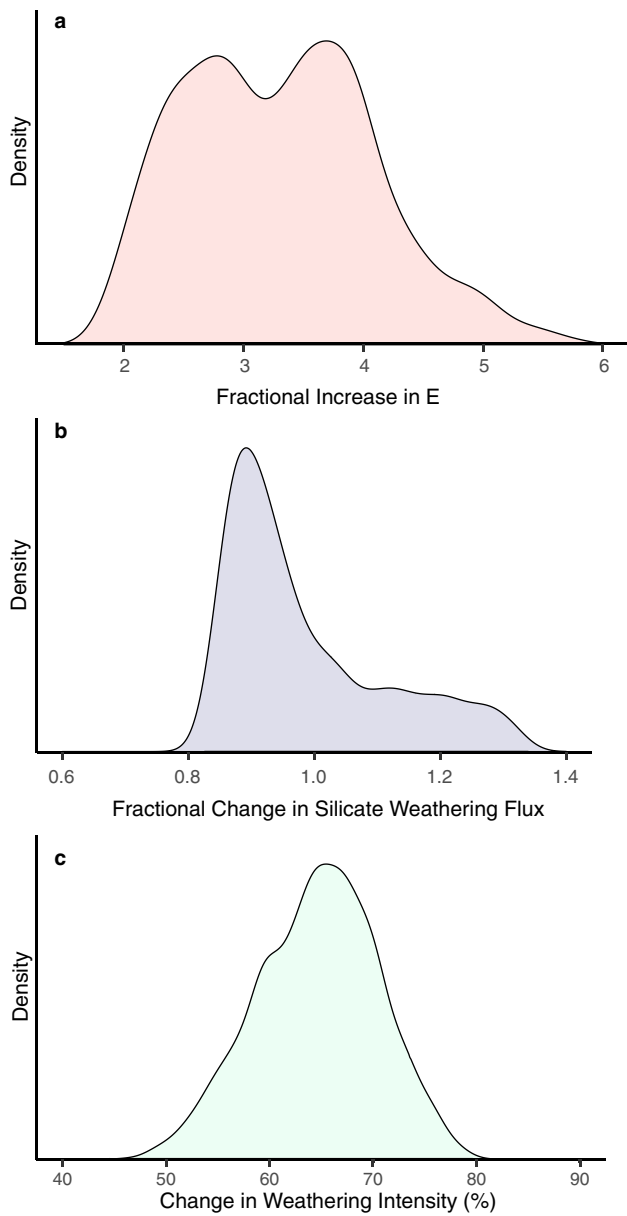
Results of the CLiBeSO-W model (including carbon and sulfur cycle fluxes, $\delta^7\text{Li}$, ${}^{10}\text{Be}/{}^9\text{Be}$, silicate weathering intensity, and E) using the mean of the parameters in the convergent simulations are included as Supplementary Information. Results of all convergent CLiBeSO-W simulations are archived in the ETH Research Collection (<https://doi.org/10.3929/ethz-b-000338022>). Additional CLiBeSO-W results and data formats can be obtained from the corresponding author on reasonable request.

Code availability

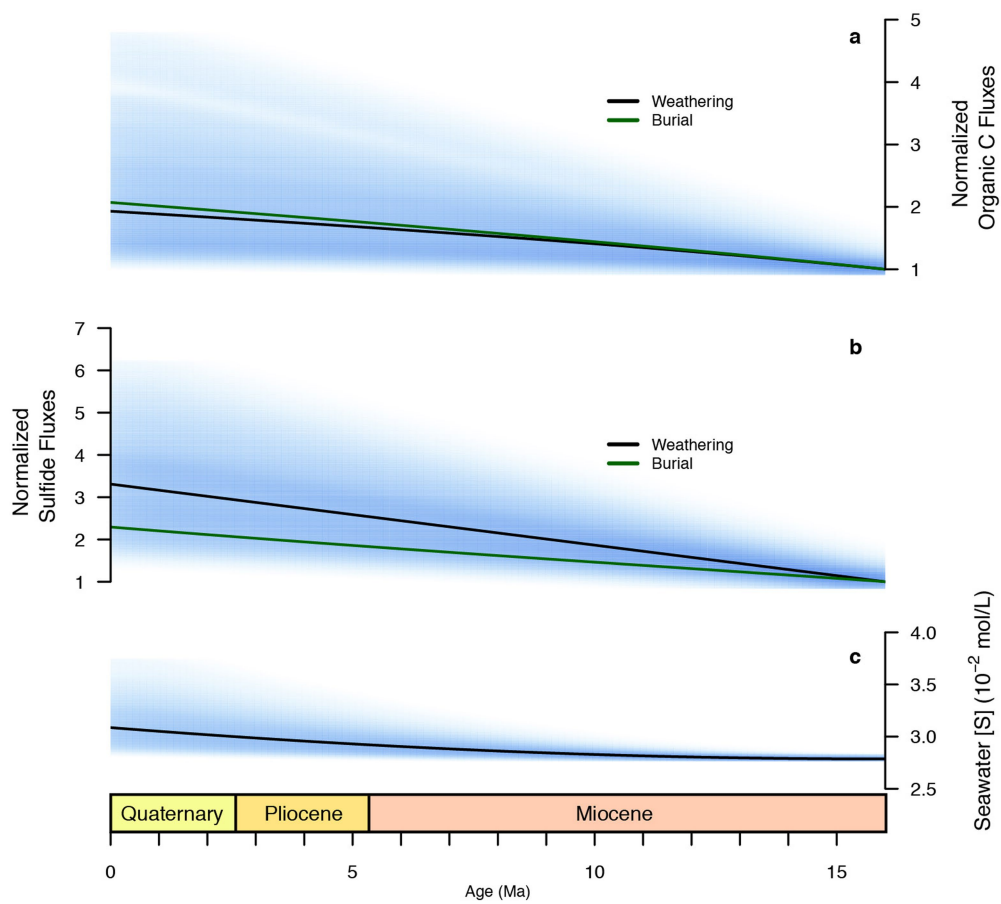
The CLiBeSO-W model is available in the Supplementary Information. Additional code (including scripts for plotting figures and the MCMC scheme) is available from the corresponding author on reasonable request.

- Bergman, N. M., Lenton, T. M. & Watson, A. J. COPSE: A new model of biogeochemical cycling over Phanerozoic time. *Am. J. Sci.* **304**, 397–437 (2004).
- Knutti, R., Rugenstein, M. A. A. & Hegerl, G. C. Beyond equilibrium climate sensitivity. *Nat. Geosci.* **10**, 727–736 (2017).
- PALAEOSSENS Project Members. Making sense of palaeoclimate sensitivity. *Nature* **491**, 683–691 (2012).
- Snyder, C. W. Evolution of global temperature over the past two million years. *Nature* **538**, 226–228 (2016).
- Galy, V., Peucker-Ehrenbrink, B. & Eglinton, T. Global carbon export from the terrestrial biosphere controlled by erosion. *Nature* **521**, 204–207 (2015).
- Hemingway, J. D. et al. Microbial oxidation of lithospheric organic carbon in rapidly eroding tropical mountain soils. *Science* **360**, 209–212 (2018).
- Bachan, A. & Kump, L. R. The rise of oxygen and siderite oxidation during the Lomagundi Event. *Proc. Natl Acad. Sci. USA* **112**, 6562–6567 (2015).
- Stolper, D. A., Bender, M. L., Dreyfus, G. B., Yan, Y. & Higgins, J. A. A Pleistocene ice core record of atmospheric O_2 concentrations. *Science* **353**, 1427–1430 (2016).
- Zeebe, R. E. & Wolf-Gladrow, D. *CO₂ in Seawater: Equilibrium, Kinetics, Isotopes* (Elsevier, 2001).
- Brennan, S. T., Lowenstein, T. K. & Cendon, D. I. The major-ion composition of Cenozoic seawater: The past 36 million years from fluid inclusions in marine halite. *Am. J. Sci.* **313**, 713–775 (2013).
- Galy, V. et al. Efficient organic carbon burial in the Bengal fan sustained by the Himalayan erosional system. *Nature* **450**, 407–410 (2007).
- Hilton, R. G. et al. Tropical-cyclone-driven erosion of the terrestrial biosphere from mountains. *Nat. Geosci.* **1**, 759–762 (2008).
- Lenton, T. M., Daines, S. J. & Mills, B. J. W. COPSE reloaded: an improved model of biogeochemical cycling over Phanerozoic time. *Earth Sci. Rev.* **178**, 1–28 (2018).
- Ridgwell, A. J. An end to the 'rain ratio' reign? *Geochem. Geophys. Geosyst.* **4**, 1051 (2003).
- Lau, K. V. et al. Marine anoxia and delayed Earth system recovery after end-Permian extinction. *Proc. Natl Acad. Sci. USA* **113**, 2360–2365 (2016).
- Payne, J. L. & Kump, L. R. Evidence for recurrent Early Triassic massive volcanism from quantitative interpretation of carbon isotope fluctuations. *Earth Planet. Sci. Lett.* **256**, 264–277 (2007).
- Torres, M. A. et al. The acid and alkalinity budgets of weathering in the Andes–Amazon system: insights into the erosional control of global biogeochemical cycles. *Earth Planet. Sci. Lett.* **450**, 381–391 (2016).
- Bolton, E. W., Berner, R. A. & Petsch, S. T. The weathering of sedimentary organic matter as a control on atmospheric O_2 : II. Theoretical modeling. *Am. J. Sci.* **306**, 575–615 (2006).
- Winnick, M. J. et al. Snowmelt controls on concentration-discharge relationships and the balance of oxidative and acid-base weathering fluxes in an alpine catchment, East River, Colorado. *Water Resour. Res.* **53**, 2507–2523 (2017).
- Calmels, D., Gaillardet, J., Brenot, A. & France-Lanord, C. Sustained sulfide oxidation by physical erosion processes in the Mackenzie River basin: climatic perspectives. *Geology* **35**, 1003–1006 (2007).
- Burke, A. et al. Sulfur isotopes in rivers: insights into global weathering budgets, pyrite oxidation, and the modern sulfur cycle. *Earth Planet. Sci. Lett.* **496**, 168–177 (2018).
- Berner, R. A. & Raiswell, R. Burial of organic carbon and pyrite sulfur in sediments over phanerozoic time: a new theory. *Geochim. Cosmochim. Acta* **47**, 855–862 (1983).

56. Maher, K. & von Blanckenburg, F. Surface ages and weathering rates from ^{10}Be (meteoric) and $^{10}\text{Be}/^9\text{Be}$: insights from differential mass balance and reactive transport modeling. *Chem. Geol.* **446**, 70–86 (2016).
57. von Blanckenburg, F., Bouchez, J., Ibarra, D. E. & Maher, K. Stable runoff and weathering fluxes into the oceans over Quaternary climate cycles. *Nat. Geosci.* **8**, 538–542 (2015).
58. Winnick, M. J. & Caves, J. K. Oxygen isotope mass-balance constraints on Pliocene sea level and East Antarctic Ice Sheet stability. *Geology* **43**, 879–882 (2015).
59. Gasson, E., DeConto, R. M. & Pollard, D. Modeling the oxygen isotope composition of the Antarctic ice sheet and its significance to Pliocene sea level. *Geology* **44**, 827–830 (2016).
60. Vigier, N. & Godderis, Y. A new approach for modeling the Cenozoic oceanic lithium isotope paleo-variations: the key role of climate. *Clim. Past* **11**, 635–645 (2015).
61. Li, G. & West, A. J. Evolution of Cenozoic seawater lithium isotopes: coupling of global denudation regime and shifting seawater sinks. *Earth Planet. Sci. Lett.* **401**, 284–293 (2014).
62. Flesch, G. D., Anderson, A. R., Jr & Svec, H. J. A secondary isotopic standard for $^6\text{Li}/^7\text{Li}$ determinations. *Int. J. Mass Spectrom. Ion Phys.* **12**, 265–272 (1973).
63. Brass, G. W. The variation of the marine $^{87}\text{Sr}/^{86}\text{Sr}$ ratio during Phanerozoic time: interpretation using a flux model. *Geochim. Cosmochim. Acta* **40**, 721–730 (1976).
64. Kump, L. R. Alternative modeling approaches to the geochemical cycles of carbon, sulfur, and strontium isotopes. *Am. J. Sci.* **289**, 390–410 (1989).
65. Bolton, C. T. et al. Decrease in coccolithophore calcification and CO_2 since the middle Miocene. *Nat. Commun.* **7**, 10284 (2016).
66. Mejía, L. M. et al. A diatom record of CO_2 decline since the late Miocene. *Earth Planet. Sci. Lett.* **479**, 18–33 (2017).
67. Super, J. R. et al. North Atlantic temperature and $p\text{CO}_2$ coupling in the early-middle Miocene. *Geology* **46**, 519–522 (2018).
68. Seki, O. et al. Alkenone and boron-based Pliocene $p\text{CO}_2$ records. *Earth Planet. Sci. Lett.* **292**, 201–211 (2010).
69. Hönisch, B., Hemming, N. G., Archer, D., Siddall, M. & McManus, J. F. Atmospheric carbon dioxide concentration across the mid-Pleistocene transition. *Science* **324**, 1551–1554 (2009).
70. Chalk, T. B. et al. Causes of ice age intensification across the Mid-Pleistocene Transition. *Proc. Natl Acad. Sci. USA* **114**, 13114–13119 (2017).
71. Sosdian, S. M. et al. Constraining the evolution of Neogene ocean carbonate chemistry using the boron isotope pH proxy. *Earth Planet. Sci. Lett.* **498**, 362–376 (2018).
72. Zhang, Y. G., Pagani, M., Liu, Z., Bohaty, S. M. & Deconto, R. A 40-million-year history of atmospheric CO_2 . *Philos. Trans. R. Soc. A* **371**, <https://doi.org/10.1098/rsta.2013.0096> (2013).
73. Pagani, M., Liu, Z., LaRiviere, J. & Ravelo, A. C. High Earth-system climate sensitivity determined from Pliocene carbon dioxide concentrations. *Nat. Geosci.* **3**, 27–30 (2010).
74. Stap, L. B. et al. CO_2 over the past 5 million years: continuous simulation and new $\delta^{13}\text{B}$ -based proxy data. *Earth Planet. Sci. Lett.* **439**, 1–10 (2016).
75. Bartoli, G., Hönisch, B. & Zeebe, R. E. Atmospheric CO_2 decline during the Pliocene intensification of Northern Hemisphere glaciations. *Paleoceanography* **26**, PA4213 (2011).
76. Martínez-Botí, M. A. et al. Plio-Pleistocene climate sensitivity evaluated using high-resolution CO_2 records. *Nature* **518**, 49–54 (2015).
77. Badger, M. P. S. et al. CO_2 drawdown following the middle Miocene expansion of the Antarctic Ice Sheet. *Paleoceanography* **28**, 42–53 (2013).
78. Badger, M. P. S., Schmidt, D. N., Mackensen, A. & Pancost, R. D. High-resolution alkenone palaeobarometry indicates relatively stable $p\text{CO}_2$ during the Pliocene (3.3–2.8 Ma). *Philos. Trans. R. Soc. A* **371**, <https://doi.org/10.1098/rsta.2013.0094> (2013).
79. Foster, G. L., Lear, C. H. & Rae, J. W. B. The evolution of $p\text{CO}_2$, ice volume and climate during the middle Miocene. *Earth Planet. Sci. Lett.* **341–344**, 243–254 (2012).
80. Greenop, R., Foster, G. L., Wilson, P. A. & Lear, C. H. Middle Miocene climate instability associated with high-amplitude CO_2 variability. *Paleoceanography* **29**, 845–853 (2014).
81. EPICA community members. Eight glacial cycles from an Antarctic ice core. *Nature* **429**, 623–628 (2004).
82. Soetaert, K., Petzoldt, T. & Setzer, R. W. Solving initial value differential equations in R: package deSolve. *J. Stat. Softw.* **33**, 1–25 (2010).
83. Wold, C. N. & Hay, W. W. Estimating ancient sediment fluxes. *Am. J. Sci.* **290**, 1069–1089 (1990).
84. McLennan, S. M. Weathering and global denudation. *J. Geol.* **101**, 295–303 (1993).
85. Milliman, J. D. & Farnsworth, K. L. *River Discharge to the Global Ocean: A Global Synthesis* (Cambridge Univ. Press, 2011).
86. Zeebe, R. E. & Caldeira, K. Close mass balance of long-term carbon fluxes from ice-core CO_2 and ocean chemistry records. *Nat. Geosci.* **1**, 312–315 (2008).
87. West, A. J., Galy, A. & Bickle, M. Tectonic and climatic controls on silicate weathering. *Earth Planet. Sci. Lett.* **235**, 211–228 (2005).
88. Millot, R., Gaillardet, J., Dupré, B. & Allégro, C. J. The global control of silicate weathering rates and the coupling with physical erosion: New insights from rivers of the Canadian Shield. *Earth Planet. Sci. Lett.* **196**, 83–98 (2002).
89. Gabet, E. J. & Mudd, S. M. A theoretical model coupling chemical weathering rates with denudation rates. *Geology* **37**, 151–154 (2009).
90. Moon, S., Chamberlain, C. P. & Hilley, G. E. New estimates of silicate weathering rates and their uncertainties in global rivers. *Geochim. Cosmochim. Acta* **134**, 257–274 (2014).
91. Milliman, J. D. & Droxler, A. W. Neritic and pelagic carbonate sedimentation in the marine environment: ignorance is not bliss. *Geol. Rundsch.* **85**, 496–504 (1996).
92. Iglesias-Rodriguez, M. D. et al. Progress made in study of ocean's calcium carbonate budget. *Eos Trans AGU* **83**, 365–375 (2002).
93. Burton, M. R., Sawyer, G. M. & Granieri, D. Deep carbon emissions from volcanoes. *Rev. Mineral. Geochem.* **75**, 323–354 (2013).
94. Wallmann, K. Controls on the Cretaceous and Cenozoic evolution of seawater composition, atmospheric CO_2 and climate. *Geochim. Cosmochim. Acta* **65**, 3005–3025 (2001).
95. Broecker, W. S. & Peng, T. H. *Tracers in the Sea* (Eldigio Press, 1982).

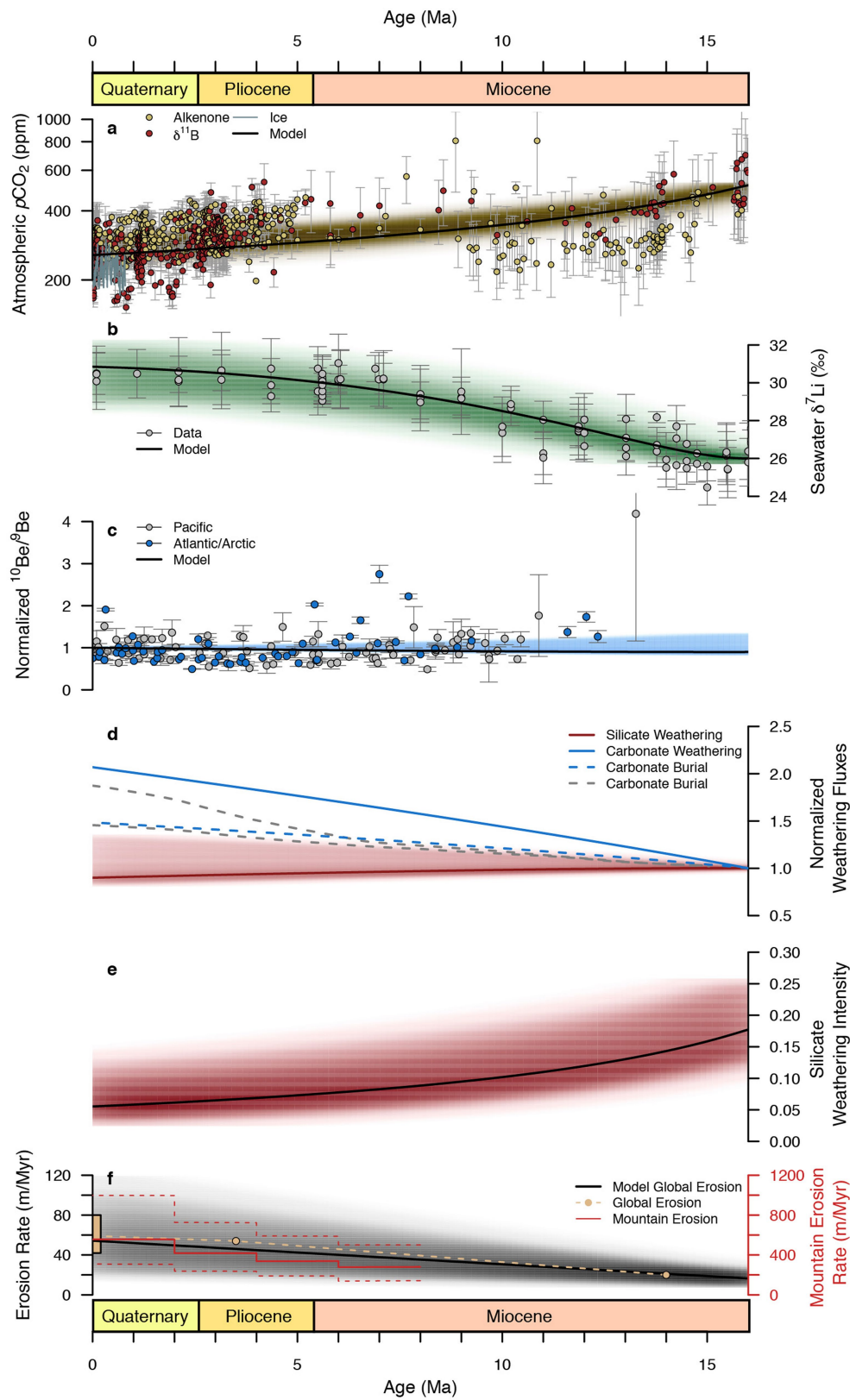


Extended Data Fig. 1 | Density plots of results from the CLiBeSO-W model. a, The increase in erosion (E/E_0) that would be required over the Neogene to simultaneously match the seawater records of $\delta^7\text{Li}$ and $^{10}\text{Be}/^9\text{Be}$ and the atmospheric p_{CO_2} record. **b,** The consequent change in the silicate weathering flux (F_{silw}) given the change in erosion in **a**. **c,** Estimated change in weathering intensity (%). The area under each curve sums to 1.



Extended Data Fig. 2 | Redox-sensitive weathering fluxes. **a**, Normalized global organic weathering (black) and burial (green) flux. The blue shading is the convergent MCMC density for the organic weathering flux.

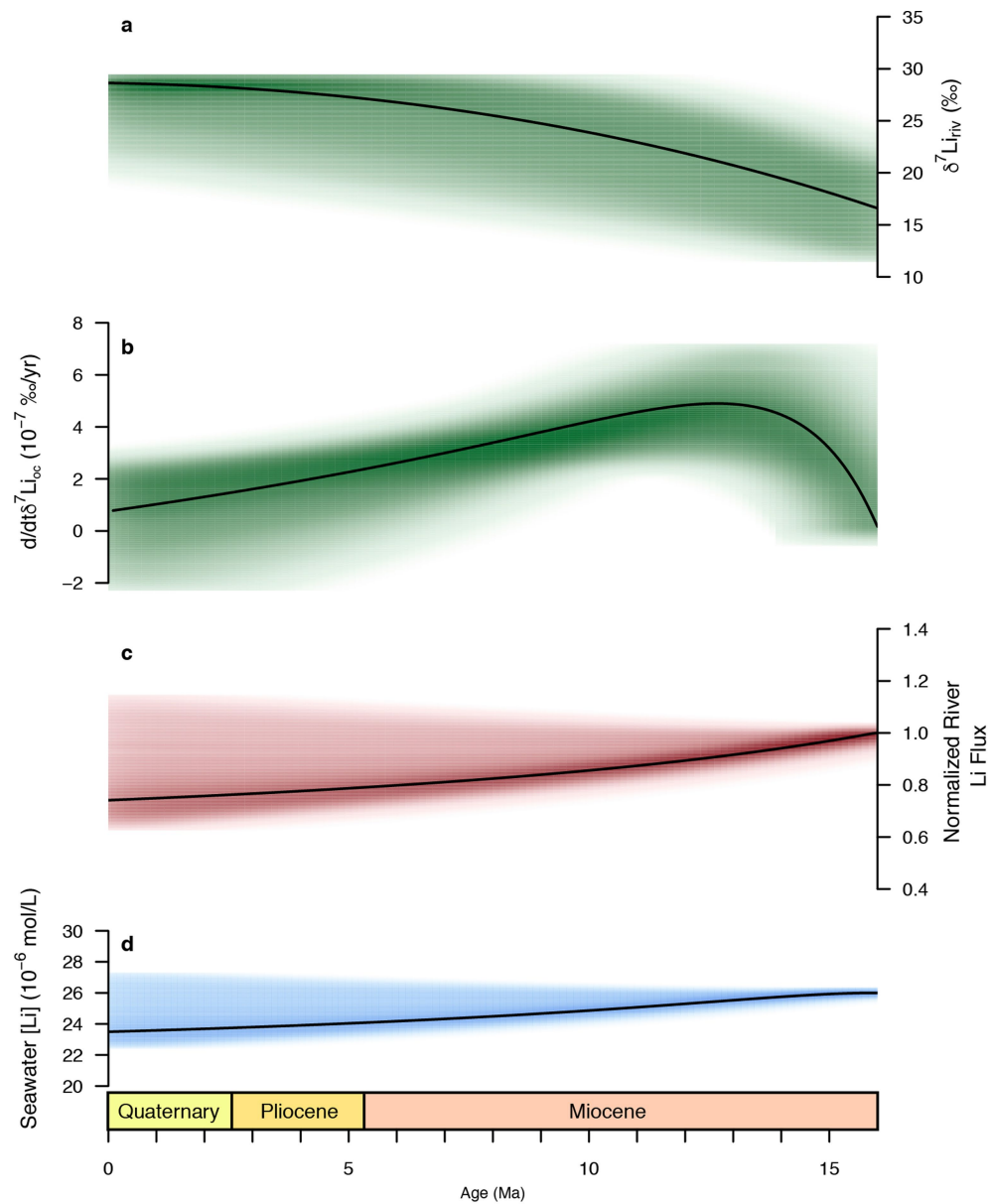
b, Normalized global sulfide weathering (black) and burial (green) flux. The blue shading is the MCMC density for the sulfide weathering flux. **c**, Seawater S concentration.



Extended Data Fig. 3 | See next page for caption.

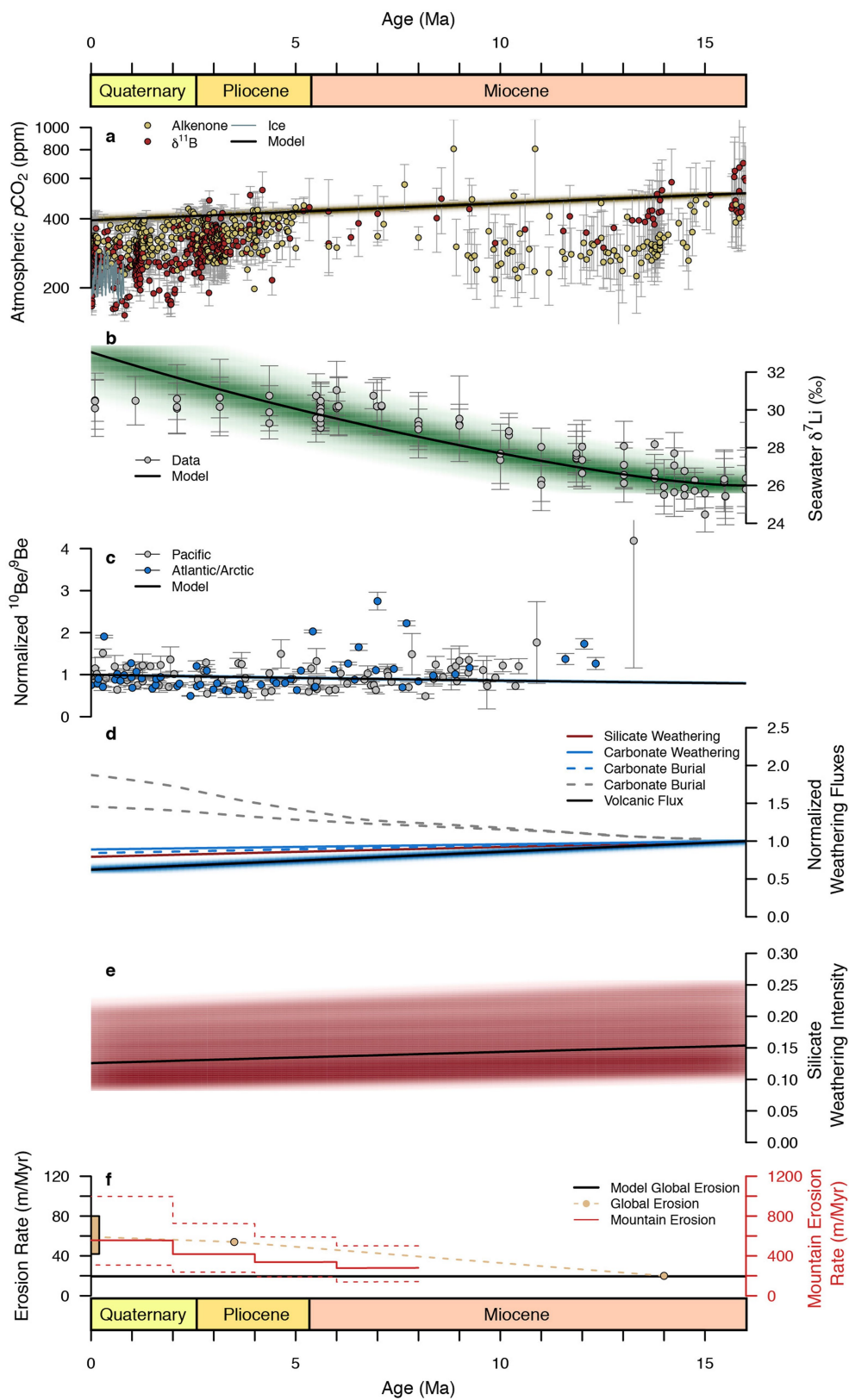
Extended Data Fig. 3 | Results from the CLiBeSO-W model when pyrite weathering is treated as invariant over the late Cenozoic. Compare with Fig. 1. Black lines show model output when using the mean of the MCMC optimized parameters, and the shading indicates the density of all convergent MCMC iterations. **a**, Atmospheric p_{CO_2} with alkenone (yellow) and $\delta^{11}\text{B}$ (red) proxy and ice-core (blue) data (see Methods). **b**, Modelled seawater $\delta^7\text{Li}$. The grey points are planktonic foraminifera $\delta^7\text{Li}$ (ref. ²⁸). **c**, Modelled marine $^{10}\text{Be}/^9\text{Be}$ normalized to the value at 0 Myr ago. The grey and blue points are reconstructed marine $^{10}\text{Be}/^9\text{Be}$ from ref. ⁷ normalized to the modern $^{10}\text{Be}/^9\text{Be}$ value of the respective ocean basin.

d, Normalized silicate (red) and carbonate (blue) weathering flux and carbonate burial (dashed blue) flux. The grey, dashed lines are the estimated minimum and maximum changes in F_{carb} from sedimentary volumes³⁰. **e**, Silicate weathering intensity. **f**, Globally averaged erosion rate (left axis). The solid red and lower and upper dashed lines show the mean, minimum and maximum mountain erosion rate estimates, respectively¹⁶ (right axis). The beige line is an estimate of global erosion rate¹⁵ and the beige bar at 0 Myr ago indicates the full range of estimated pre-anthropogenic erosion rates^{15,18} (left axis). In **a–c**, error bars are the published uncertainty for the data (minimum/maximum in **a**, 1σ in **b**, **c**).



Extended Data Fig. 4 | Results of the embedded lithium cycle model.
a, Global river $\delta^7\text{Li}$. **b**, Change in seawater $\delta^7\text{Li}$ ($d/dt \delta^7\text{Li}$). **c**, Normalized river flux of Li. **d**, Seawater Li concentration. In all panels, the shading

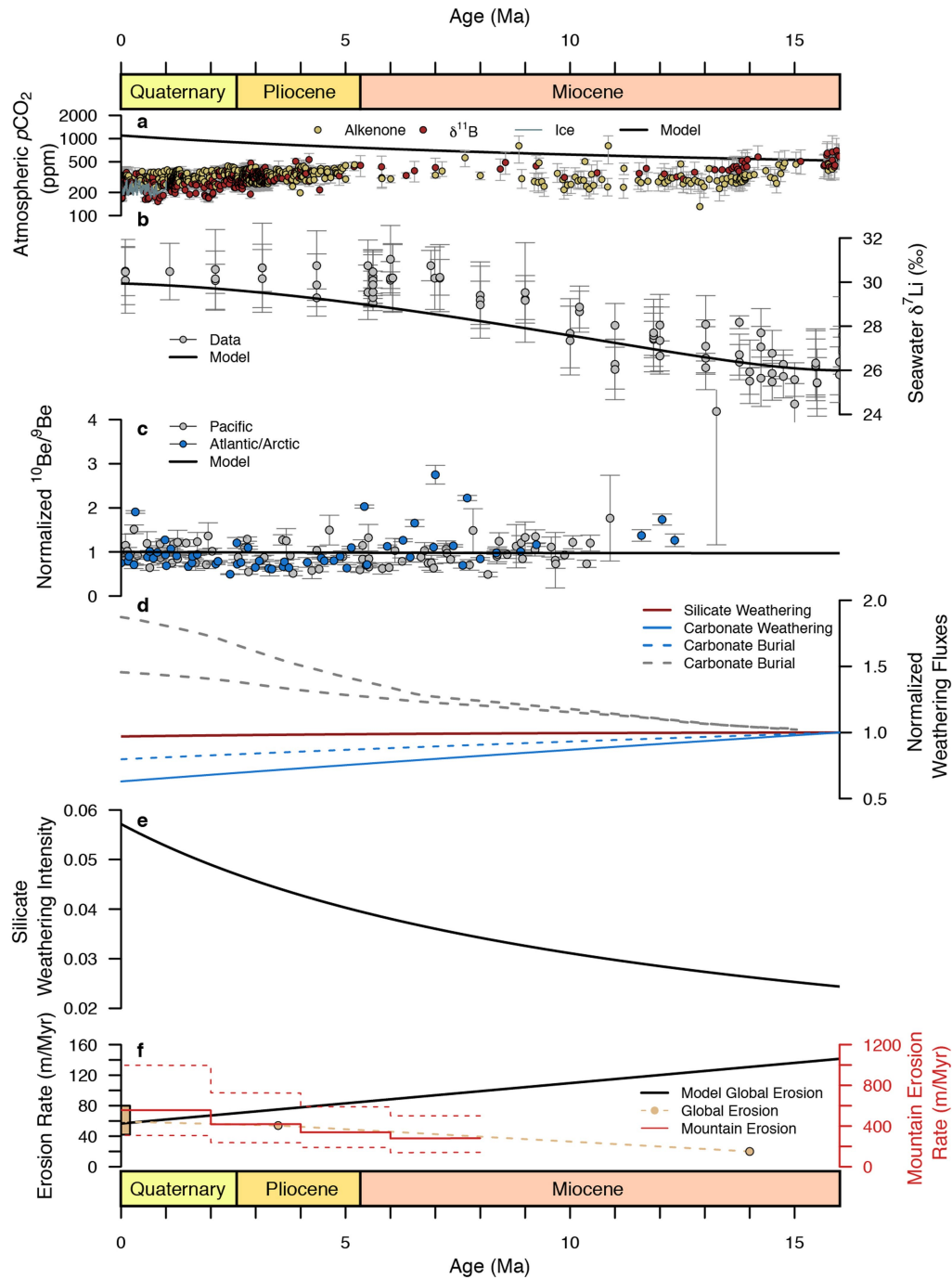
indicates relative density of convergent MCMC iterations, with darker colours indicating more iterations. The solid line is the result using the mean of the optimized parameters.



Extended Data Fig. 5 | See next page for caption.

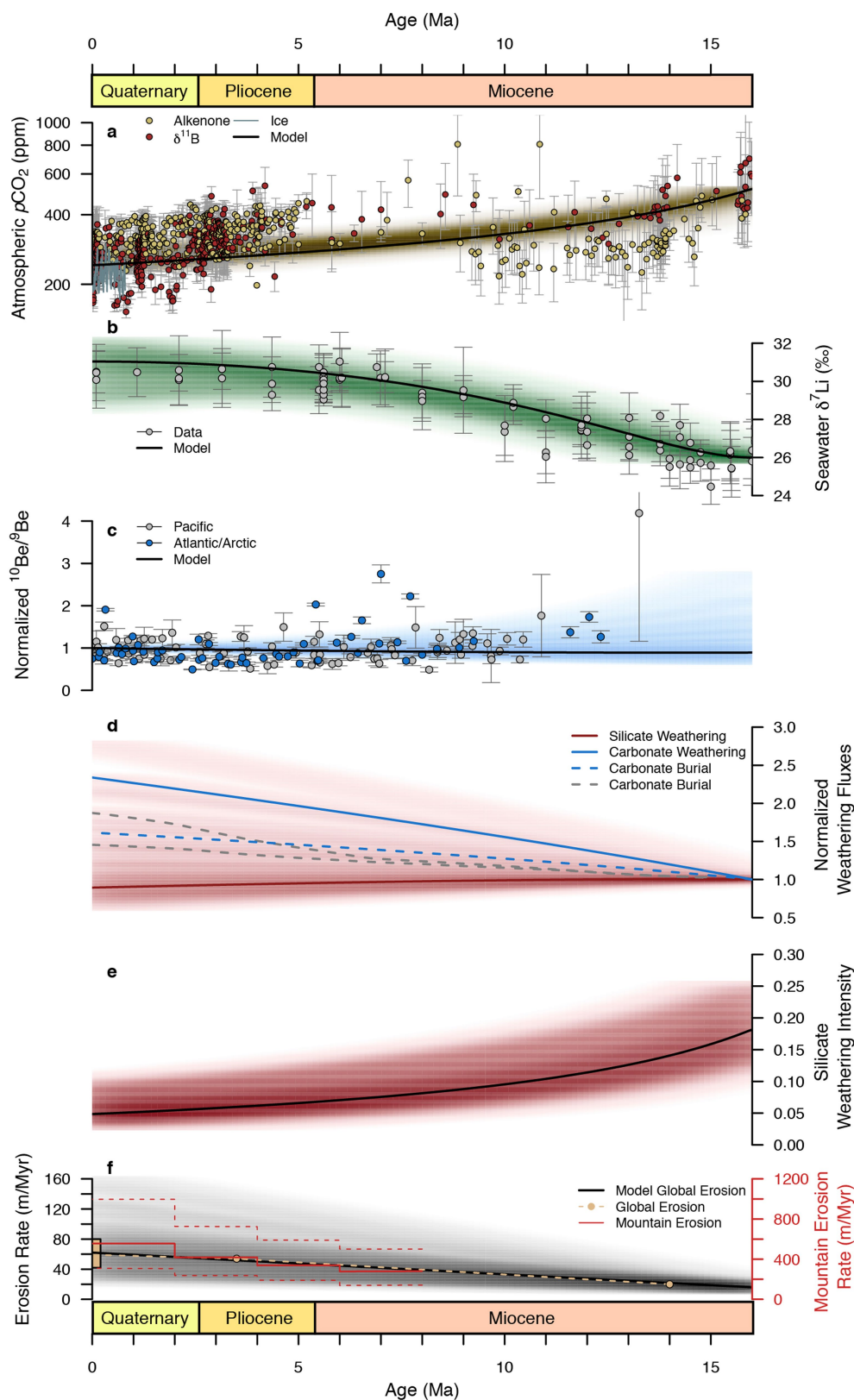
Extended Data Fig. 5 | CLiBeSO-W results assuming that only the volcanic and solid Earth degassing flux varies and erosion remains constant. Here, F_{volc} is permitted to vary to optimize the fit with the data, resulting in a 37% decrease in F_{volc} (full range: 35–41% decrease). Compare with Fig. 1. The model output is shown by black lines using mean of the MCMC optimized parameters and the shading indicates density of all convergent MCMC iterations. **a**, Atmospheric P_{CO_2} with alkenone (yellow) and $\delta^{11}\text{B}$ (red) proxy and ice-core (blue) data (see Methods). **b**, Modelled seawater $\delta^7\text{Li}$. The grey points are planktonic foraminifera $\delta^7\text{Li}$ (ref. 28). **c**, Modelled marine $^{10}\text{Be}/^9\text{Be}$ normalized to the value at 0 Myr ago. The grey and blue points are reconstructed marine $^{10}\text{Be}/^9\text{Be}$ from ref. 7 normalized to the modern $^{10}\text{Be}/^9\text{Be}$ value of the respective ocean basin.

d, Normalized silicate (red) and carbonate (blue) weathering flux, carbonate burial (dashed blue) flux, and volcanic/solid Earth degassing flux (black with blue shading). The grey, dashed lines are the estimated minimum and maximum changes in F_{carb} from sedimentary volumes³⁰. **e**, Silicate weathering intensity. **f**, Globally averaged erosion rate (left axis). The solid red and lower and upper dashed lines show the mean, minimum and maximum mountain erosion rate estimates, respectively¹⁶ (right axis). The beige line is an estimate of the global erosion rate¹⁵ and the beige bar at 0 Myr ago indicates the full range of estimated pre-anthropogenic erosion rates^{15,18} (left axis). In **a–c**, error bars are published uncertainty for the data (minimum/maximum in **a**, 1σ in **b**, **c**).



Extended Data Fig. 6 | CLiBeSO-W model results if erosion decreases and the initial silicate weathering intensity 16 Myr ago is less than 0.05. Here, erosion decreases by 60% and the initial silicate weathering intensity is set to 0.024. **a**, Atmospheric $p\text{CO}_2$ with alkenone (yellow) and $\delta^{11}\text{B}$ (red) proxy and ice-core (blue) data (see Methods). **b**, Modelled seawater $\delta^7\text{Li}$. The grey points are planktonic foraminifera $\delta^7\text{Li}$ (ref. ²⁸). **c**, Modelled marine $^{10}\text{Be}/^9\text{Be}$ normalized to the value at 0 Myr ago. The grey and blue points are reconstructed marine $^{10}\text{Be}/^9\text{Be}$ from ref. ⁷ normalized to the modern $^{10}\text{Be}/^9\text{Be}$ value of the respective ocean basin. **d**, Normalized silicate (red) and carbonate (blue) weathering flux and carbonate burial

(dashed blue) flux. The grey, dashed lines are estimated minimum and maximum changes in F_{carb} from sedimentary volumes³⁰. **e**, Silicate weathering intensity. **f**, Globally averaged erosion rate (left axis). The solid red and lower and upper dashed lines show the mean, minimum and maximum mountain erosion rate estimates¹⁶, respectively (right axis). The beige line is an estimate of global erosion rate¹⁵ and the beige bar at 0 Myr ago indicates the full range of estimated pre-anthropogenic erosion rates^{15,18} (left axis). In **a**–**c**, error bars are published uncertainty for the data (minimum/maximum in **a**, 1σ in **b**, **c**).



Extended Data Fig. 7 | CLiBeSO-W model results when marine $^{10}\text{Be}/^9\text{Be}$ data are excluded from the MCMC inversion. a, Atmospheric p_{CO_2} with alkenone (yellow) and $\delta^{11}\text{B}$ (red) proxy and ice-core (blue) data (see Methods). **b,** Modelled seawater $\delta^7\text{Li}$. The grey points are planktonic foraminifera $\delta^7\text{Li}$ (ref. 28). **c,** Modelled marine $^{10}\text{Be}/^9\text{Be}$ normalized to the value at 0 Myr ago. The grey and blue points are reconstructed marine $^{10}\text{Be}/^9\text{Be}$ from ref. 7 normalized to the modern $^{10}\text{Be}/^9\text{Be}$ value of the respective ocean basin. **d,** Normalized silicate (red) and carbonate (blue) weathering flux and carbonate burial (dashed blue) flux. The grey, dashed lines are the estimated minimum and maximum changes in F_{carb} from

sedimentary volumes³⁰. **e,** Silicate weathering intensity. **f,** Globally averaged erosion rate (left axis). The solid red and lower and upper dashed lines show the mean, minimum and maximum mountain erosion rate estimates¹⁶, respectively (right axis). The beige line is an estimate of global erosion rate¹⁵ and the beige bar at 0 Myr ago indicates the full range of estimated pre-anthropogenic erosion rates^{15,18} (left axis). In **a–c**, error bars are published uncertainty for the data (minimum/maximum in **a**, 1σ in **b**, **c**). The model output is shown by black lines, using the mean of the MCMC optimized parameters and the shading indicates the density of all convergent MCMC iterations.

Extended Data Table 1 | Parameters used in the CLiBeSO-W model and the range of values in perturbed initial parameters of the MCMC runs

Parameters	Optimized Values	Range of Values used in MCMC	Units	Source
Ocean Volume	1.4	–	10 ²¹ L	Refs. 9,86
Salinity	35	–	psu	
Earth System Sensitivity	6	3–9	°C/CO ₂ doubling	Ref. 35,37
α_{sil}	0.55	0.33–0.7	–	Refs. 24,87–89
α_{carb}	0.86	0.7–1	–	Ref. 24
α_{orgw}	0.55	0.3–0.9	–	Ref. 24,39
α_{orgb}	0.26	0.1–0.4	–	Ref. 38,44,45
k_{sil}	13.2	–	10 ¹² mol C/yr	
k_{carb}	13.2	–	10 ¹² mol C/yr	
<i>Initial values of time-varying parameters</i>				
E/F_{silw} Ratio	4.6	3–40	–	Ref. 21
pCO ₂	517	–	ppm	Ref. 65–67
pH	8	–	–	
<i>Initial Fluxes and Reservoirs</i>				
$F_{silw,0}$	13.2	–	10 ¹² mol C/yr	Refs. 33,90
$F_{carbw,0}$	13.2	–	10 ¹² mol C/yr	Ref. 33
$F_{orgw,0}$	13.2	–	10 ¹² mol C/yr	Refs. 9,94
$F_{sulfw,0}$	0.5	–	10 ¹² mol S/yr	Refs. 12,34,53
$F_{carbb,0}$	26.4	–	10 ¹² mol C/yr	Refs. 30,91,92
$F_{orgb,0}$	13.2	–	10 ¹² mol C/yr	
$F_{sulfb,0}$	0.5	–	10 ¹² mol S/yr	
$F_{volc,0}$	13.2	–	10 ¹² mol C/yr	Ref. 93,94
Ocean S Reservoir	3.9	–	10 ¹⁹ mol S	Ref. 95
<i>Li Cycle Parameters and Fluxes</i>				
$F_{w,Li}$	8.5	–	10 ⁹ mol Li/yr	Ref. 61
$F_{h,Li}$	13	–	10 ⁹ mol Li/yr	Ref. 61
$F_{ba,Li}$	10.5	–	10 ⁹ mol Li/yr	Ref. 61
$F_{rw,Li}$	11	–	10 ⁹ mol Li/yr	Ref. 61
Seawater [Li]	26	–	10 ⁻⁴ mol Li/L	Ref. 61
Initial δ^7Li_{oc}	26	–	‰	Ref. 28
δ^7Li_h	8.3	–	‰	Ref. 61
Δ_{ba}	12.54	9.3–16.3	‰	
Δ_{rw}	17	–	‰	Ref. 61
Δ_{sec}	17	–	‰	Ref. 22
a	4.5	–	–	
b	0.575	–	–	
δ^7Li_{rock}	1.5	–	‰	Ref. 27

Refs 9,12,21,22,24,27,28,30,33–35,37–39,44,45,53,61,65–67,86–95

Optimized values are calculated using the mean parameter value for the convergent MCMC runs. Only parameters that were varied as part of the MCMC runs are listed in the third column. The value of Δ_{ba} is varied to ensure isotopic steady-state in the Li system. When calculating the ratio of E/F_{silw} , F_{silw} is in units of $t yr^{-1}$ (see Methods).